



# Fe<sub>x</sub>Se<sub>y</sub>@C superlattice nanocrystals for peroxymonosulfate activation: Intrinsic nature of Fe spin state

Qiang Zhong<sup>a,b</sup>, Yue Sun<sup>a</sup>, Chenmin Xu<sup>a</sup>, Yanfang Li<sup>a</sup>, Dunyu Sun<sup>a</sup>, Leliang Wu<sup>a</sup>, Shaogui Yang<sup>a,c,\*</sup>, Yazhi Liu<sup>a</sup>, Chengdu Qi<sup>a</sup>, Zhe Xu<sup>a</sup>, Huan He<sup>a</sup>, Shiyin Li<sup>a</sup>, Zunyao Wang<sup>d</sup>, Shaobin Wang<sup>e,\*\*</sup>

<sup>a</sup> School of Environment, Jiangsu Province Engineering Research Center of Environmental Risk Prevention and Emergency Response Technology, Jiangsu Engineering Lab of Water and Soil Eco-remediation, Nanjing Normal University, Nanjing, Jiangsu 210023, PR China

<sup>b</sup> School of Geography, Nanjing Normal University, Nanjing, Jiangsu 210023, PR China

<sup>c</sup> Suzhou Furong Environmental engineering Co., Ltd

<sup>d</sup> State Key Laboratory of Pollution Control and Resources Reuse, School of Environment, Nanjing University, Nanjing, Jiangsu 210023, PR China

<sup>e</sup> School of Chemical Engineering, The University of Adelaide, Adelaide, SA 5005, Australia

## ARTICLE INFO

### Keywords:

Peroxymonosulfate activation

Spin state

Superlattice

Iron-based selenides

Intrinsic activity

## ABSTRACT

Two-dimensional layered carbon-coated Fe<sub>x</sub>Se<sub>y</sub> nanocrystal superlattices with different crystalline structure (2D Fe<sub>x</sub>Se<sub>y</sub>@C NS) are prepared and tested in Fenton-like reaction via PMS activation. The intrinsic nature and properties that govern the activity of 2D Fe<sub>x</sub>Se<sub>y</sub>@C NS are deeply elucidated. Experimental analysis and theoretical calculations indicated that the spin state of Fe strongly decided the catalytic activity of 2D Fe<sub>x</sub>Se<sub>y</sub>@C NS, and that a high spin state of Fe (4.16 μ<sub>B</sub>) with a large effective magnetic moment not only regulated PMS adsorption (−3.06 eV) for increasing electronic density (0.79 e), but also accelerated interfacial charge transfer for HSO<sub>5</sub><sup>−</sup> decomposition to produce SO<sub>4</sub><sup>•−</sup>. Therefore, among 2D Fe<sub>x</sub>Se<sub>y</sub>@C NS, 2D FeSe<sub>2</sub>@C NS exhibited the most active performance in PMS activation with brilliant durability and adaptability. The study illustrates a new application of superlattice nanomaterials in environmental remediation and supplies fundamental insight to the intrinsic chemical structure of Fe-based catalysts for PMS activation.

## 1. Introduction

Peroxymonosulfate (PMS)-based advanced oxidation processes (AOPs) are one of the most effective water treatment technologies for tackling persistent organic contaminants [1–3]. Among various PMS activation methods, a heterogeneous iron-based catalyst has become an optimal selection due to its low energy requirement, no secondary pollution, and operational convenience [4,5]. Although abundant iron-based nanomaterials have been developed and employed in PMS-based AOPs [6,7], evident drawbacks such as poor stability, slow reaction kinetics, low active site exposure, and indistinct catalytic mechanisms have been observed. Hence, it is highly desirable to design a novel iron-based catalyst with high efficiency and stability.

Among various iron-based catalysts, iron-based selenides (Fe<sub>x</sub>Se<sub>y</sub>) exhibit distinct advantages and are promising candidates for PMS

activation by the strong electronic interaction and synergetic effect between iron and selenium [8,9]. Besides, to further promote the reaction kinetics of PMS, defect engineering has been developed to improve the intrinsic activity of Fe<sub>x</sub>Se<sub>y</sub> [8]. However, the previous strategy still exhibits some problems, such as a complex preparation process with a low yield (a batch experiment yielded only a few dozen milligrams of the catalyst) and less exposure of active sites. Recently, self-assembled nanocrystal superlattices (NS) have received sustained attention in various fields due to design flexibility, long-range ordered structure, and tunable coupling interactions, which can jointly improve the physicochemical properties and stability over the disordered/agglomerated counterparts [10–12]. Moreover, organic ligand derived carbon at the surface of nanocrystals can lead to an interconnected carbon network, which will extremely improve structural stability, accelerate electron transfer, and reduce metal ion leaching of NS [13,14]. More

\* Corresponding author at: School of Environment, Jiangsu Province Engineering Research Center of Environmental Risk Prevention and Emergency Response Technology, Jiangsu Engineering Lab of Water and Soil Eco-remediation, Nanjing Normal University, Nanjing, Jiangsu 210023, PR China.

\*\* Corresponding author.

E-mail addresses: [yangsg@njnu.edu.cn](mailto:yangsg@njnu.edu.cn) (S. Yang), [shaobin.wang@adelaide.edu.au](mailto:shaobin.wang@adelaide.edu.au) (S. Wang).

<https://doi.org/10.1016/j.apcatb.2023.123113>

Received 6 March 2023; Received in revised form 15 July 2023; Accepted 17 July 2023

Available online 18 July 2023

0926-3373/© 2023 Elsevier B.V. All rights reserved.

importantly, two dimensional (2D) porous NS can markedly improve mass transfer and exposure of catalytic sites [10,15], which deeply affect their application in catalysis. Therefore, carbon-coated 2D  $\text{Fe}_x\text{Se}_y$  NS with porous and easily accessible structures have a great promise for environmental catalysis. Whereas, building  $\text{Fe}_x\text{Se}_y$  superlattice materials remains a substantial challenge. Moreover, few superlattice systems have been investigated in the sulfate radical ( $\text{SO}_4^{\cdot-}$ ) based advanced oxidation processes (SR-AOPs) thus far.

One remarkable feature of iron-based selenides for PMS activation with high efficiency is often attributed to synergies between Fe and Se [8,9,16,17–19]. Nevertheless, the intrinsic origin of the high activity, i. e., the atomic/quantum scale mechanism underpinning the efficient Fe redox recycling in  $\text{Fe}_x\text{Se}_y$ , is elusive and neglected. Notably, a Fe-Se system exhibits various stable polymorphs including FeSe,  $\text{FeSe}_2$ ,  $\text{Fe}_3\text{Se}_4$ , and  $\text{Fe}_7\text{Se}_8$  under ambient conditions [20]. In addition, previous studies have reported that the physicochemical properties of  $\text{Fe}_x\text{Se}_y$  in a Fe-Se system are closely related to a Fe-Se elemental ratio as well as crystal structure [21–23]. Therefore, besides enhancing the catalytic activity of  $\text{Fe}_x\text{Se}_y$  for PMS activation, it is also essential to discern the activity order of different  $\text{Fe}_x\text{Se}_y$  crystals to entail a fundamental insight into the catalytic mechanisms. Nevertheless, less attention has been paid to  $\text{Fe}_x\text{Se}_y$  catalysts with different crystal structure and to disclosing the structure-activity relationship.

In this work, we synthesized a series of 2D carbon-coated  $\text{Fe}_x\text{Se}_y$  NS composed of different structured crystals (2D  $\text{Fe}_x\text{Se}_y$ @C NS,  $x:y = 1:1$ ,  $1:2$ ,  $3:4$ ,  $7:8$ ) via a spatially constrained topochemical transformation process, using carbon-coated  $\text{Fe}_3\text{O}_4$  NS as a precursor, and evaluated their performance in Fenton-like reaction via PMS activation for degradation of pharmaceutical and personal care products (PPCPs). Particularly, the 2D porous NS favor the generation of catalytic sites and mass transport, meanwhile the carbon framework boosts the electron transfer and mechanical strength during catalytic oxidation. By a comprehensive investigation from experimental analyses and theoretical calculations, we identified the spin state of the Fe active center as the decisive factor defining the catalytic activity of 2D  $\text{Fe}_x\text{Se}_y$ @C NS for PMS activation. Intriguingly, a stronger super-exchange electron interaction between Fe and Se renders higher spin states of the Fe site in 2D  $\text{FeSe}_2$  @C NS than that in 2D  $\text{FeSe}$ @C NS, 2D  $\text{Fe}_3\text{Se}_4$  @C NS, and 2D  $\text{Fe}_7\text{Se}_8$  @C NS, thus resulting in higher catalytic activation performance of the 2D  $\text{FeSe}_2$  @C NS. This study opens a scalable and versatile route for preparation of 2D  $\text{Fe}_x\text{Se}_y$ @C NS and discloses the intrinsic mechanism of 2D  $\text{Fe}_x\text{Se}_y$ @C NS for PMS activation, which will stimulate design and oriented regulation of superior catalysts for future environmental remediation.

## 2. Experimental sections

### 2.1. Chemicals and reagents

The detailed materials are presented in Text S1 of the Supporting Information (SI).

### 2.2. Synthesis of 2D $\text{Fe}_3\text{O}_4$ @C NS

In a typical synthesis process, 0.36 g  $\text{FeCl}_3 \cdot 6\text{H}_2\text{O}$ , 1 mL deionized water, and 1.22 g of Na-oleate were mixed thoroughly. The resulting mixture was aged at 85 °C for 3 h, and then mixed with 20 g of  $\text{Na}_2\text{SO}_4$  powder, which acts as a template to prevent complex agglomeration during annealing. Finally, the above mixture was subjected to calcination at 600 °C under  $\text{N}_2$  atmosphere for 3 h. After cooling down to room temperature,  $\text{Na}_2\text{SO}_4$  crystals were removed by washing with deionized water. The resulting product was dried at 60 °C for 24 h in a vacuum oven prior to further use.

### 2.3. Synthesis of 2D $\text{Fe}_x\text{Se}_y$ @C NS

For 2D  $\text{FeSe}$ @C NS, the as-obtained 2D  $\text{Fe}_3\text{O}_4$  @C NS and Se powder in a mass ratio of 1:6 were put at the opposite corners of a quartz boat. Subsequently, the quartz boat was transferred into a tube furnace and selenization was executed at 600 °C for 3 h under an atmosphere of  $\text{H}_2/\text{Ar}$  (5 vol% of  $\text{H}_2$ ) gas with a heat rate of 2 °C  $\text{min}^{-1}$ . Afterward, 2D  $\text{FeSe}$ @C NS were obtained.

For 2D  $\text{FeSe}_2$  @C NS, the as-obtained 2D  $\text{Fe}_3\text{O}_4$  @C NS and Se powder in a different mass ratio (1:3) were put at the opposite corners of a quartz boat. Subsequently, the quartz boat was transferred into a tube furnace and selenization was executed at certain temperature (300, 360, 400 °C) for 8 h under an atmosphere of  $\text{H}_2/\text{Ar}$  (5 vol% of  $\text{H}_2$ ) gas with a heat rate of 2 °C  $\text{min}^{-1}$ . Afterward, 2D  $\text{FeSe}_2$  @C NS were obtained.

For 2D  $\text{Fe}_3\text{Se}_4$  @C NS, the as-obtained 2D  $\text{Fe}_3\text{O}_4$  @C NS and Se powder in a mass ratio of 1:3 were put at the opposite corners of a quartz boat. Subsequently, the quartz boat was transferred into a tube furnace and selenization was executed at 350 °C for 1 h and subsequent 450 °C for 2 h under an atmosphere of  $\text{H}_2/\text{Ar}$  (5 vol% of  $\text{H}_2$ ) gas with a heat rate of 2 °C  $\text{min}^{-1}$ . Afterward, 2D  $\text{Fe}_3\text{Se}_4$  @C NS were obtained.

For 2D  $\text{Fe}_7\text{Se}_8$  @C NS, the as-obtained 2D  $\text{Fe}_3\text{O}_4$  @C NS and Se powder in a mass ratio of 1:7.5 were put at the opposite corners of a quartz boat. Subsequently, the quartz boat was transferred into a tube furnace and selenization was executed at 450 °C for 4 h and subsequent 600 °C for 2 h under an atmosphere of  $\text{H}_2/\text{Ar}$  (5 vol% of  $\text{H}_2$ ) gas with a heat rate of 2 °C  $\text{min}^{-1}$ . Afterward, 2D  $\text{Fe}_7\text{Se}_8$  @C NS were obtained.

### 2.4. Characterization of the catalysts

The crystal structure of the synthesized catalysts was investigated by X-ray diffraction spectroscopy (XRD) using a Rigaku Miniflex-600 diffractometer operated at 40 kV and 15 mA with Cu K $\alpha$  radiation ( $\lambda = 1.5406$  Å). The material morphologies were observed by field emission scanning electron microscopy (SEM, Hitachi SU8200) and transmission electron microscopy (TEM, Hitachi H7700) at an acceleration voltage of 100 kV. In addition, the material microstructures were examined by high-resolution TEM (HRTEM, Talos F200X) operated at 200 kV. Atomic force microscopy images (AFM) were obtained by a Bruker ICON2-SYS scanning probe microscope under a tapping mode. Surface potential distributions of the as-prepared samples were measured by the Kelvin probe force microscopy (KPFM) in a scanning probe microscopy (SPM) system. The Brunauer-Emmett-Teller (BET) specific surface areas of the catalysts were measured by the  $\text{N}_2$  adsorption-desorption method on a Builder 4200 instrument. The valent states of the metals were analyzed by X-ray photoelectron spectroscopy (XPS) on a Thermo ESCALAB 250 analyzer equipped with an Al K $\alpha$  ( $h\nu=1486.6$  eV) X-ray source. Inductively coupled plasma atomic emission spectroscopy (ICP-AES) was employed to determine Se and Fe contents. Raman and in-situ Raman measurements were carried out on a Raman spectrometer (HORIBA-800) with a 514 nm laser as the excitation source. Zero field cooled (ZFC) and field cooled (FC) measurements were executed by a magnetic property measurement system (MPMS-3, Quantum Design) under  $H=1$  kOe for temperature-dependent (2–400 K) magnetization measurements.  $\text{H}_2$  temperature-programmed reduction ( $\text{H}_2$ -TPR),  $\text{NH}_3$  temperature-programmed desorption ( $\text{NH}_3$ -TPD), and  $\text{O}_2$  temperature-programmed desorption ( $\text{O}_2$ -TPD) were performed using a micromeritics AutoChem II 2920 analyzer. Electron paramagnetic resonance (EPR) spectra of trapping radicals were obtained by a Bruker E500 EPR device.

### 2.5. Electrochemical measurements

The detailed electrochemical measurements were given in Text S2 of SI.



## 2.6. Theoretical calculation methods

The detailed calculation methods were given in Text S3 of SI.

## 2.7. Catalytic performance evaluation

The activities of catalysts for PMS activation and pollutant degradation were evaluated by using diatrizoic acid (DTZ) as a model recalcitrant pollutant. All experiments were carried out in 50 mL flat-bottom beaker containing 50 mL of DTZ solution (10 mg/L) at room temperature ( $25 \pm 2^\circ\text{C}$ ). After adding a catalyst (5 mg) into a DTZ solution, magnetic stirring (15 min) was immediately applied to ensure a uniform suspension and sufficient adsorption-desorption equilibrium. Then, a predetermined amount of PMS was added to initiate the reaction, and the pH of the reaction solution was not adjusted artificially and fluctuated within a range of 2.9–3.4 in most cases after addition of PMS. The reaction solution was regularly sampled (0.8 mL of the suspension was withdrawn at predetermined time intervals during the reaction) and

immediately added with methanol to cease the reaction. The samples after filtration through  $0.22\ \mu\text{m}$  nylon membranes were subjected to DTZ concentration measurements. All the experiments were carried out in duplicate or triplicate. In addition, the DTZ concentration was measured by high-performance liquid chromatography (HPLC, 1290, Agilent Inc.) with a Kromasil C18 column ( $4.6 \times 250\ \text{mm}$ ,  $5\ \mu\text{m}$ ) at the detection wavelength of  $254\ \text{nm}$ . A mixture of 0.1% formic acid water solution/methanol (90/10, vol/vol) at a flow rate of  $1.0\ \text{mL}\cdot\text{min}^{-1}$  was used as the mobile phase. The degradation intermediates of DTZ were identified by liquid chromatography high resolution mass spectrometry with a source of HESI (HESI-LC-HRMS Thermo Scientific Q Exactive). The gradient program of the mobile phase is shown in Fig. S1 at a flow rate of  $0.5\ \text{mL}\cdot\text{min}^{-1}$ . The total organic carbon (TOC) concentration was determined by a Shimadzu TOC-VCPh analyzer.

The kinetic rate constants ( $k_{\text{obs}}$ ) of DTZ degradation were calculated according to the pseudo-first-order kinetic model (Eq. (1)):

$$\ln(C_0/C_t) = k_{\text{obs}} \cdot t \quad (1)$$

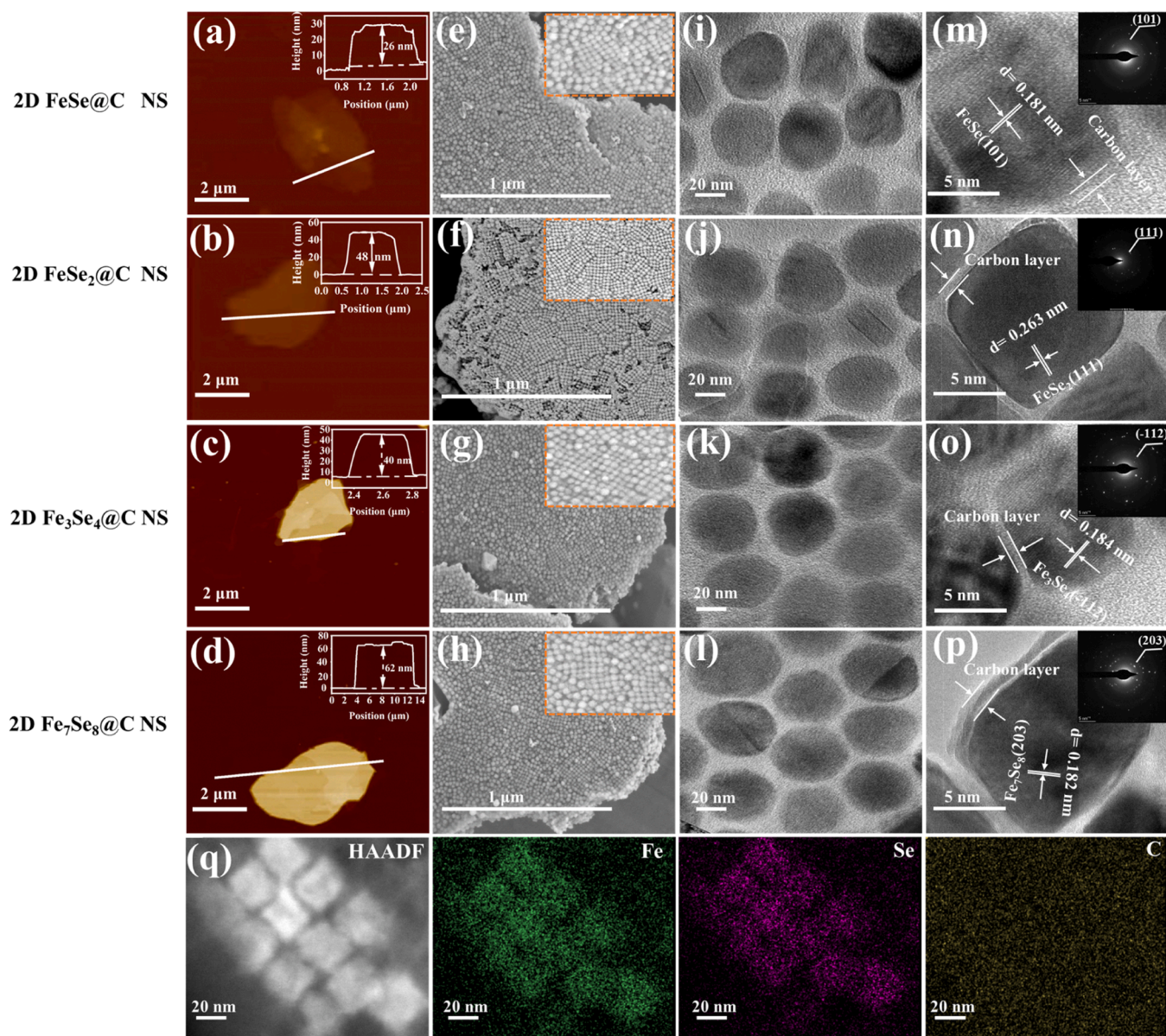


**Fig. 1.** Morphology of the different iron-based selenide catalysts. AFM images (inset is the height profile of catalysts) (a, b, c, d), scanning electron microscopy (SEM) and its magnification (inset) (e, f, g, h), transmission electron microscopy (TEM) (i, j, k, l), high-resolution TEM (HRTEM) (inset: FFT image) (m, n, o, p), (q) STEM image and corresponding elemental mapping of 2D FeSe<sub>2</sub>@C NS.

where  $C_t$  is the DTZ concentration at certain reaction time ( $t$ ),  $C_0$  is the initial DTZ concentration, and  $k_{obs}$  is the first-order kinetic rate constant ( $\text{min}^{-1}$ ). Moreover, it is worth noting that the pH value of the reaction system was not further adjusted unless otherwise stated. To avoid any misleading conclusions, buffers were not used. In a recycling test, the catalyst was collected after each run, fully washed with ethanol and water and dried before the next test.

### 3. Results and discussions

#### 3.1. Synthesis and characterizations

2D superlattices comprising of carbon-coated  $\text{Fe}_3\text{O}_4$  nanocrystals are synthesized from thermal decomposition of Fe-oleate on  $\text{Na}_2\text{SO}_4$  surfaces [24] (Fig. S2(a-b)). Details of the morphology properties for 2D  $\text{Fe}_3\text{O}_4$  @ C NS are displayed in Fig. S3(a-i). Particularly, the as-prepared 2D  $\text{Fe}_3\text{O}_4$  @ C NS are employed as the precursor for subsequent growth of 2D  $\text{Fe}_x\text{Se}_y$ @C NS via one-step selenization (Fig. S4). During the selenization reaction, isolated  $\text{Fe}_3\text{O}_4$  nanocrystals confined in a carbon framework are transformed into 2D  $\text{Fe}_x\text{Se}_y$ @C NS via the nanoscaled Kirkendall diffusion effect, and retain the ordered structure. Notably, the phases of 2D  $\text{Fe}_x\text{Se}_y$ @C NS can be tailored via adjusting the amount of selenium powder and calcination temperature.

Atomic force microscopy (AFM, Fig. 1(a-d)) reveals that the

thickness of 2D  $\text{Fe}_x\text{Se}_y$ @C NS is remarkably decreased as compared to the 2D  $\text{Fe}_3\text{O}_4$  @ C NS precursor. In addition, 2D  $\text{Fe}_x\text{Se}_y$ @C NS exhibit similar physicochemical properties in morphology (Fig. 1(e-l)), hydrophilicity (Fig. S5 (a-d)), and Fe content (Table S1). Interestingly, after acid etching of embedded  $\text{Fe}_x\text{Se}_y$  nanocrystals (i.e.,  $\text{FeSe}_2$  nanocrystals), the hollow 2D carbon nanostructure retained undamaged, revealing its mechanical rigidity and structure stability (Fig. S6(a)). Besides, 2D carbon framework can be evenly dispersed in aqueous solution, ensuring fully contacting with the aqueous solution (Fig. S6(b)). Notably, the interconnected carbon framework not only boosts transfer of electrons, but also greatly improves durability of the catalyst [25]. In addition, 2D  $\text{FeSe}_2$  @C NS show good thermal stability up to 280 °C (Fig. S7). HRTEM with fast Fourier transform (FFT) images (Fig. 1(m-p) and inset) verify that 2D  $\text{Fe}_x\text{Se}_y$ @C NS are highly crystalline. The  $d$ -spacing of 0.181, 0.263, 0.184, and 0.182 nm can be attributed to the (101) plane of 2D  $\text{FeSe}$ @C NS, (111) plane of 2D  $\text{FeSe}_2$  @C NS, ( $-112$ ) plane of 2D  $\text{Fe}_3\text{Se}_4$  @C NS, and (203) plane of 2D  $\text{Fe}_7\text{Se}_8$  @C NS, respectively. Moreover, STEM with energy-dispersive X-ray spectroscopy (EDS) mapping reveal homogeneous distributions of Fe, Se, and C elements throughout 2D  $\text{FeSe}_2$  @C NS (Fig. 1(q)). Notably, the current synthetic process can be easily scaled up (Fig. S8(a-d)) without any solvent and allows synthesis of different iron selenides via controlling the temperature (Fig. 2(a) and Fig. S9) and can be easily extended to prepare other iron-based compounds (Fig. S10).

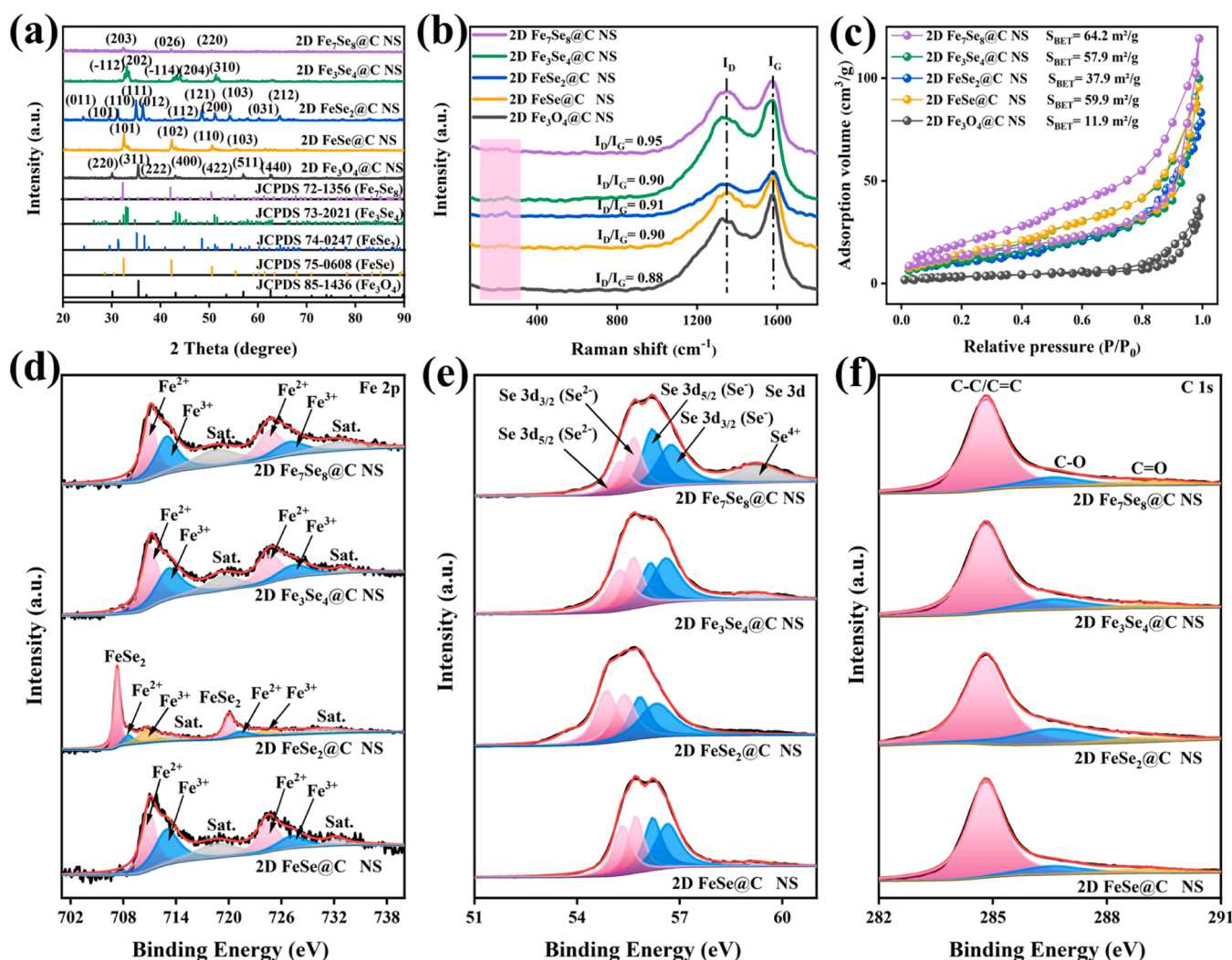


Fig. 2. (a) XRD patterns, (b) Raman spectra, (c)  $\text{N}_2$  adsorption/desorption isotherms, and high-resolution XPS spectra of the as-prepared catalysts (d) Fe 2p, (e) Se 3d, and (f) C 1s.



The crystal structures of 2D  $\text{Fe}_3\text{O}_4$ @C NS and 2D  $\text{Fe}_x\text{Se}_y$ @C NS were detected by X-ray diffraction (XRD). In Fig. 2(a), 2D  $\text{Fe}_3\text{O}_4$ @C NS exhibit diffraction peaks indexed to  $\text{Fe}_3\text{O}_4$  (JCPDS No. 85–1436) [10]. After one step of selenization at different temperature, 2D  $\text{FeSe}$ @C NS, 2D  $\text{FeSe}_2$ @C NS, 2D  $\text{Fe}_3\text{Se}_4$ @C NS, and 2D  $\text{Fe}_7\text{Se}_8$ @C NS display the matching diffraction peaks with tetragonal  $\text{FeSe}$  (JCPDS No. 75–0608) [26], orthorhombic  $\text{FeSe}_2$  (JCPDS No. 74–0247) [27], monoclinic  $\text{Fe}_3\text{Se}_4$  (JCPDS No. 73–2021) [28], and hexagonal  $\text{Fe}_7\text{Se}_8$  (JCPDS No. 72–1356) [29], respectively. Besides, the as-prepared catalysts show a high purity without the characteristic peaks of  $\text{Fe}_3\text{O}_4$ .

Raman spectra are displayed in Figs. 2(b) and S11. Compared with 2D  $\text{Fe}_3\text{O}_4$ @C NS, three new characteristic peaks at 181.2, 219.8, and  $254.9\text{ cm}^{-1}$  are observed. The peaks at 181.2 and  $254.9\text{ cm}^{-1}$  correspond to the Se-Se librational and stretching vibrations or their combination, and the peak at  $219.8\text{ cm}^{-1}$  is attributed to the Se-Se stretching vibrations [30,31]. Furthermore, two strong peaks at  $\sim 1580$  and  $\sim 1350\text{ cm}^{-1}$  correspond to G and D bands of carbon, respectively, and similar  $I_D/I_G$  values can be observed in 2D  $\text{Fe}_x\text{Se}_y$ @C NS catalysts [32], indicating that the selenization of 2D  $\text{Fe}_3\text{O}_4$ @C NS exhibited a rather limited influence on the carbon network. Moreover, as shown in Fig. 2(c), 2D  $\text{Fe}_x\text{Se}_y$ @C NS exhibit prominent characteristics of type-IV isotherms with a H2 hysteresis loop, demonstrating the existence of a microporous/mesoporous structure [33]. Notably, the surface area and pore size (Fig. S12(a)) of 2D  $\text{Fe}_x\text{Se}_y$ @C NS are higher than those of the parent 2D  $\text{Fe}_3\text{O}_4$ @C NS, presumably due to the porous nature of the constituent particles. The large specific surface area and pore volume are conducive to offering abundant catalytic sites and boosting mass transfer in a catalytic reaction [25,34].

The valence state and composition of the as-synthesized catalysts are further surveyed by X-ray photoelectron spectroscopy (XPS). XPS displays existence of C, Fe, Se in 2D  $\text{Fe}_x\text{Se}_y$ @C NS (Fig. S12(b)). As shown in Fig. 2(d), the high-resolution Fe 2p spectra indicate coexistence of  $\text{Fe}^{3+}$

and  $\text{Fe}^{2+}$  in 2D  $\text{FeSe}$ @C NS, 2D  $\text{Fe}_3\text{Se}_4$ @C NS, and 2D  $\text{Fe}_7\text{Se}_8$ @C NS [26,28,29]. The peaks at 720.2 and 707.3 eV can be assigned to  $\text{Fe } 2p_{1/2}$  and  $\text{Fe } 2p_{3/2}$  of  $\text{FeSe}_2$ , respectively [8,35]. Notably, the other peaks in 2D  $\text{FeSe}_2$ @C NS can be attributed to oxidized Fe species on the surface. However, no iron oxides could be found in the XRD, reflecting little oxidation on the catalyst surface. Interestingly, compared with 2D  $\text{FeSe}$ @C NS, 2D  $\text{Fe}_3\text{Se}_4$ @C NS, and 2D  $\text{Fe}_7\text{Se}_8$ @C NS, 2D  $\text{FeSe}_2$ @C NS show a significant shift of Fe 2p peaks towards lower binding energies, reflecting stronger Fe, Se interaction for the Fe sites to gain charges. The high-resolution Se 3d spectra of 2D  $\text{Fe}_x\text{Se}_y$ @C NS show three selenium species i.e., monoselenide ( $\text{Se}^-$ ), selenide ( $\text{Se}^{2-}$ ), and selenate ( $\text{Se}^{4+}$ ) [20]. Besides, C 1s spectra display three main peaks at 288.9, 286.5, and 284.8 eV, which are ascribed to the C=O, C-O, and C-C/C=C, respectively [11,36]. Therefore, it is suggested successful synthesis of 2D  $\text{Fe}_x\text{Se}_y$ @C NS with different crystal structure.

### 3.2. Catalytic evaluation

The as-obtained catalysts were tested in the degradation of diatrizoic acid (DTZ, Fig. S13), one of pharmaceutical and personal care products (PPCPs) widely detected in the actual aquatic environment [37]. As shown in Fig. 3(a), all the as-prepared catalysts displayed negligible adsorption and PMS itself could hardly degrade DTZ, demonstrating that the DTZ degradation is primarily ascribed to the catalytic oxidation. Notably, the DTZ degradation rate in the 2D  $\text{FeSe}_2$ @C NS/PMS (100% with 20 min) was higher than that in 2D  $\text{FeSe}_2$ @C NS/peroxydisulfate (PDS) (29.5% with 20 min) and 2D  $\text{FeSe}_2$ @C NS/hydrogen peroxide ( $\text{H}_2\text{O}_2$ ) (23.1% with 20 min) (Fig. S14), reflecting that PMS molecules are more likely to interact with the catalyst. Moreover, the catalyst exhibited the highest DTZ degradation rate constant ( $k_{\text{obs}}$ ) of  $0.169\text{ min}^{-1}$  (Fig. S15(a-b)), which is 4.8 and 9.4 times higher than phosphating and tellurization of 2D  $\text{Fe}_3\text{O}_4$ @C NS. Besides, the  $k_{\text{obs}}$  of

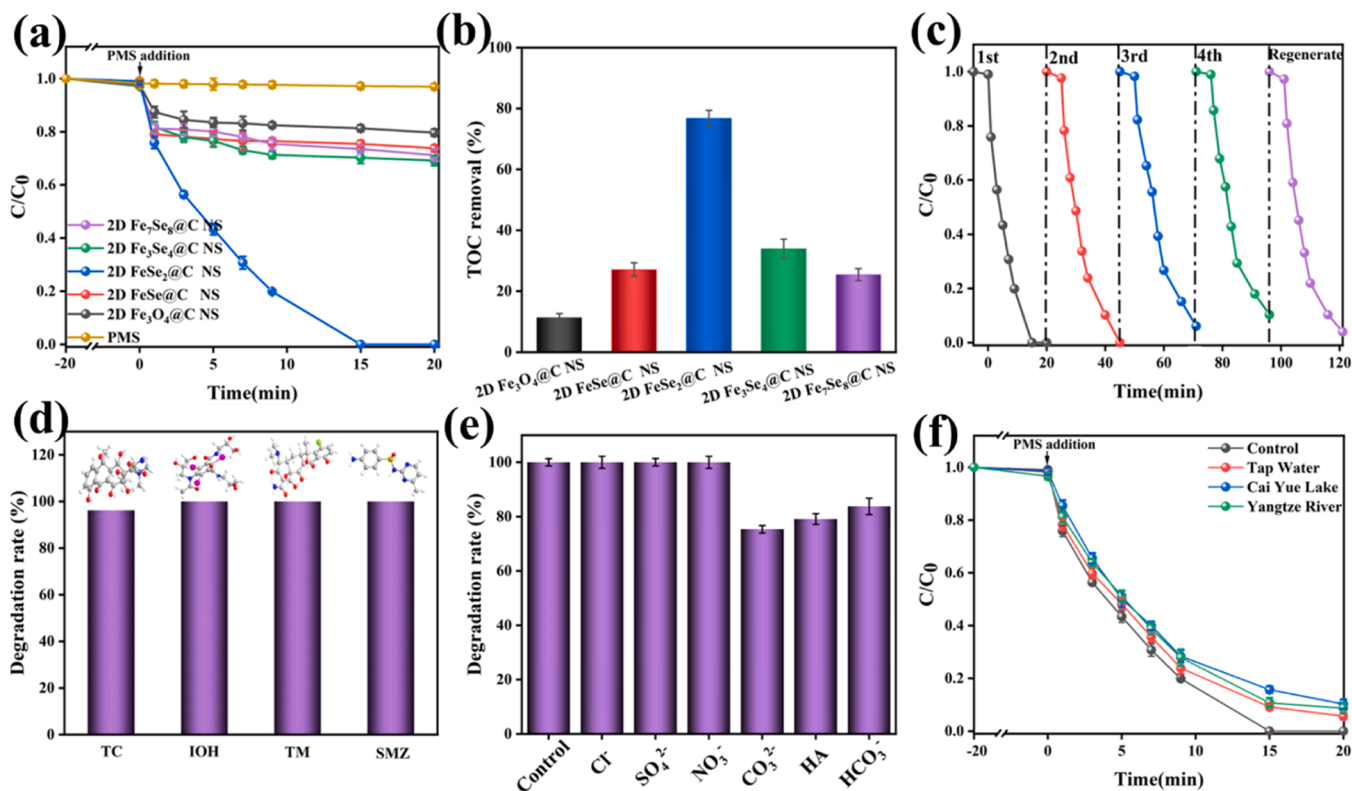


**Fig. 3.** (a) Degradation profiles of DTZ for different catalysts, (b) TOC removal of pollutants by different catalysts, (c) reuse of 2D  $\text{FeSe}_2$ @C NS catalyst, (d) degradation of multiple contaminants by 2D  $\text{FeSe}_2$ @C NS catalyst (inset: the structures of the corresponding organic contaminants), (e) effects of coexisting ions on DTZ degradation, (f) DTZ degradation efficiency in different sourced water by 2D  $\text{FeSe}_2$ @C NS-activated PMS. Experimental conditions:  $[\text{catalyst}]_0 = 0.1\text{ g/L}$ ,  $[\text{PMS}]_0 = 1.0\text{ mM}$ ,  $[\text{DTZ}]_0 = 10.0\text{ mg/L}$ .

2D FeSe<sub>2</sub>@C NS displays 24.1 times higher than that of 2D Fe<sub>3</sub>O<sub>4</sub>@C NS, indicating that anions of the catalysts play a crucial role in the catalytic activity. However, superlattice carbon exhibits rather limited degradation of DTZ (Fig. S16), indicating that Fe<sub>x</sub>Se<sub>y</sub> is the main active component. Notably, among 2D Fe<sub>x</sub>Se<sub>y</sub>@C NS, 2D FeSe<sub>2</sub>@C NS exhibited the most active performance with the maximum rate (100% with 20 min) and  $k_{obs}$  (0.169 min<sup>-1</sup>) (Fig. S17).

Meanwhile, to verify the activity difference among 2D Fe<sub>x</sub>Se<sub>y</sub>@C NS, we further employed iohexol (IOH) and tetracycline (TC) as target pollutants to be degraded in the reaction system (Fig. S18(a-b)). A similar order of IOH and TC degradation efficiency was also observed, and a similar trend can also be obtained from DTZ mineralization rates (Fig. 3(b)), suggesting that such an activity distinction stems from the catalyst inherent properties. PMS activation primarily occurs on the active sites of catalyst surface, and the reaction reactivity greatly relies on the exposed area of the catalyst surface [38]. Interestingly, the specific surface areas of 2D FeSe@C NS, 2D Fe<sub>3</sub>Se<sub>4</sub>@C NS, and 2D Fe<sub>7</sub>Se<sub>8</sub>@C NS are larger than that of 2D FeSe<sub>2</sub>@C NS (Fig. 2(c)), reflecting that more active sites are exposed, but their catalytic degradation rates of an organic matter are still sluggish and much lower (Fig. 3(a)). Similar phenomena can be obtained from the selenium vacancies and catalytic degradation properties (Fig. S19). More importantly, the similar physicochemical properties of 2D Fe<sub>x</sub>Se<sub>y</sub>@C NS including material morphology, hydrophilicity, and Fe content were excluded as the primary factors influencing the intrinsic catalytic activity of 2D Fe<sub>x</sub>Se<sub>y</sub>@C NS. Therefore, the different catalytic activities of 2D Fe<sub>x</sub>Se<sub>y</sub>@C NS are mainly ascribed to the crystal structure of Fe-Se systems and it is highly desirable to further clarify the essential structure-activity relationship between the catalytic activity and crystal structure of iron-based selenides.

Moreover, the stability of 2D FeSe<sub>2</sub>@C NS in the DTZ degradation was tested (Fig. 3(c)). The degradation efficiency of DTZ slightly declines while still remains at a high level (>95% with 20 min) after four tests. The decline is mainly attributed to the coverage of the reactive sites on the catalyst by degradation intermediates of DTZ. To test this hypothesis, we washed the catalyst with ethanol, used again, and then found that the degradation rate of DTZ was recovered. Besides, the acceptable Fe and Se leaching can be observed based on ICP-AES (Fig. S20(a)). This low ion dissolution may be ascribed to the fact that FeSe<sub>2</sub> is confined by porous carbon, which can greatly reduce ion dissolution and improve the long-term stability of the catalyst. The XRD, XPS, and SEM analyses (Fig. S20(b-d)) display no noticeable disparity in chemical composition and morphology of fresh and used 2D FeSe<sub>2</sub>@C NS, further indicating its excellent structural stability. Moreover, the homogeneous Fe<sup>2+</sup>/PMS system (Fig. S21) exhibits a limited contribution to DTZ removal, revealing the DTZ degradation by 2D FeSe<sub>2</sub>@C NS followed a heterogeneous catalytic route. In addition, the effects of catalyst dosage and concentration of PMS are provided in SI Fig. S22(a-b).

Fig. 3(d) displays that other recalcitrant organics can also be rapidly removed in 2D FeSe<sub>2</sub>@C NS/PMS system. Besides, 2D FeSe<sub>2</sub>@C NS can activate PMS for the degradation of DTZ effectively in a pH range of 3.4–10.8 (Fig. S23). Notably, the system displays superior interference resistance with various inorganic/organic anions (Fig. 3(e)). Though excess CO<sub>3</sub><sup>2-</sup>, HCO<sub>3</sub><sup>-</sup>, and humic acid (HA) display slight inhibition, high activity of the catalyst (>75% DTZ degradation within 20 min) still remains. Additionally, it also displays amazing catalytic activity in tap, lake, and real river water, achieving > 90% DTZ removal within 20 min in all these cases (Fig. 3(f)). Moreover, 2D FeSe<sub>2</sub>@C NS exhibit the exceptionally high catalytic activity, which is compelling in comparison with other metal-based catalysts used in heterogeneous PMS-based Fenton-like reactions (Table S2). In summary, 2D FeSe<sub>2</sub>@C NS can activate PMS to display remarkable activity, adaptability, and stability for remediation of wastewater.

### 3.3. DTZ reactive site evaluation and degradation pathway

The Fukui function of DTZ according to DFT calculation is employed to predict the susceptibility of DTZ by radical attack [39] (Fig. 4(a-c)). In addition, based on the UPLC-MS spectra, Fig. S24 displayed detected degradation intermediates. Notably, the highest occupied molecular orbital (HOMO) also indicates the sites that can easily escape charges. Fig. 4(b) displays that the HOMO of DTZ is mainly located on the benzene ring, branched iodine atom, and branched imino group, which can be regarded as the reactive sites attacked by ·OH/SO<sub>4</sub><sup>·-</sup>. Besides, Fukui index ( $f^0$ ) further indicates electrophilic attack of DTZ [40]. As depicted in Fig. 4(c), C2 ( $f^0 = 0.027391$ ), C3 ( $f^0 = 0.029891$ ), C5 ( $f^0 = 0.029917$ ), C6 ( $f^0 = 0.027379$ ), I10 ( $f^0 = 0.250511$ ), I11 ( $f^0 = 0.201209$ ), O15 ( $f^0 = 0.027852$ ), and I16 ( $f^0 = 0.250457$ ) with a high Fukui index are the most reactive sites [41].

In the DTZ degradation process, the degradation reaction triggered by SO<sub>4</sub><sup>·-</sup>/·OH primarily occurs through six mechanisms: amide hydrolysis, deiodination reaction, oxidation of C-OH, demethylation reaction, dehydroxylation, and deamination reaction. Therefore, four degradation pathways of DTZ are proposed (Fig. 4(d)). Firstly,  $m/z$ -616.73 [M+H]<sup>+</sup>,  $m/z$ -616.46 [M+H]<sup>+</sup>,  $m/z$ -503.04 [M+H]<sup>+</sup>, and  $m/z$ -530.84 [M+H]<sup>+</sup> can be generated via oxidation of C-OH, deiodination reaction, and amide hydrolysis. In pathway I,  $m/z$ -181.91 [M+H]<sup>+</sup> was formed via amide hydrolysis, deiodination reaction, demethylation reaction, dehydroxylation, and deamination reaction processes, which was in accordance with theoretical calculation. Similarly,  $m/z$ -312.17 [M+H]<sup>+</sup> and  $m/z$ -291 [M+H]<sup>+</sup> can be generated through a series of deep oxidation reactions in route II and route III, respectively. Notably, for pathway IV,  $m/z$ -262.03 [M+H]<sup>+</sup>,  $m/z$ -191.01 [M+H]<sup>+</sup> and  $m/z$ -138.93 [M+H]<sup>+</sup> can be rapidly formed through amide hydrolysis and deiodination reaction because of the highly active sites of I10, I11, I16, C2, C3, C5, and C6. Meanwhile,  $m/z$ -122.59 [M+H]<sup>+</sup> also could be gained via dihydroxylation. Finally, for deep oxidation in four processes, small molecules of organic compounds will be produced and eventually mineralized into CO<sub>2</sub> and H<sub>2</sub>O [42]. Therefore, it can be concluded that the proposed technology is a valid method for mineralization of degraded intermediates.

### 3.4. Identification of catalytic centers and reactive species

The reactive oxygen species (ROS) in 2D FeSe<sub>2</sub>@C NS/PMS systems were investigated by radical trapping experiments. Four scavengers, methyl alcohol (MeOH), tert-butanol (TBA), L-histidine and 4-hydroxy-2,2,6,6-tetramethylpiperidine-N-oxyl (TEMPO), were introduced into the reaction system, which can specifically quench SO<sub>4</sub><sup>·-</sup>, ·OH, <sup>1</sup>O<sub>2</sub> and O<sub>2</sub><sup>·-</sup>, respectively [8,39,43]. As depicted in Fig. 5(a), DTZ degradation was drastically restrained by methanol, while it was only moderately suppressed by TBA, L-histidine, and TEMPO, reflecting SO<sub>4</sub><sup>·-</sup> as the primary ROS in DTZ degradation.

To further verify radical products, we conducted the electron paramagnetic resonance (EPR) analysis via employing 2,2,6,6-tetramethylpiperidine (TEMP, <sup>1</sup>O<sub>2</sub> trapping agent) and 5,5-dimethyl-2-pyrrolidone-N-oxyl (DMPO, ·OH, SO<sub>4</sub><sup>·-</sup>, and O<sub>2</sub><sup>·-</sup> trapping agent) as trapping agents [44]. No characteristic peak was detected for PMS alone (Fig. 5(b)). However, DMPO-·OH and DMPO-SO<sub>4</sub><sup>·-</sup> signals became stronger in the mixture of PMS and 2D FeSe<sub>2</sub>@C NS and then faded upon DTZ addition. Moreover, the DMPO-SO<sub>4</sub><sup>·-</sup> peaks are markedly higher than those of DMPO-·OH, corresponding to the quenching results. Notably, the trivial variation in DMPO-O<sub>2</sub><sup>·-</sup> and TEMP-<sup>1</sup>O<sub>2</sub> indicates a small part of O<sub>2</sub><sup>·-</sup> and <sup>1</sup>O<sub>2</sub> involved in the DTZ degradation (Fig. 5(c-d)). Hence, it can be concluded that DTZ degradation was mainly attributed to SO<sub>4</sub><sup>·-</sup>, while slightly to ·OH, <sup>1</sup>O<sub>2</sub>, and O<sub>2</sub><sup>·-</sup>.

In addition, 2D FeSe<sub>2</sub>@C NS lead to stronger signals (SO<sub>4</sub><sup>·-</sup>, ·OH, <sup>1</sup>O<sub>2</sub>, and O<sub>2</sub><sup>·-</sup>) than 2D FeSe@C NS, 2D Fe<sub>3</sub>Se<sub>4</sub>@C NS, and 2D Fe<sub>7</sub>Se<sub>8</sub>@C NS in the ROS capture (Figs. 5(e) and S25(a-b)), and the intensity of characteristic signals for ROS in 2D Fe<sub>x</sub>Se<sub>y</sub>@C NS follows the same PMS

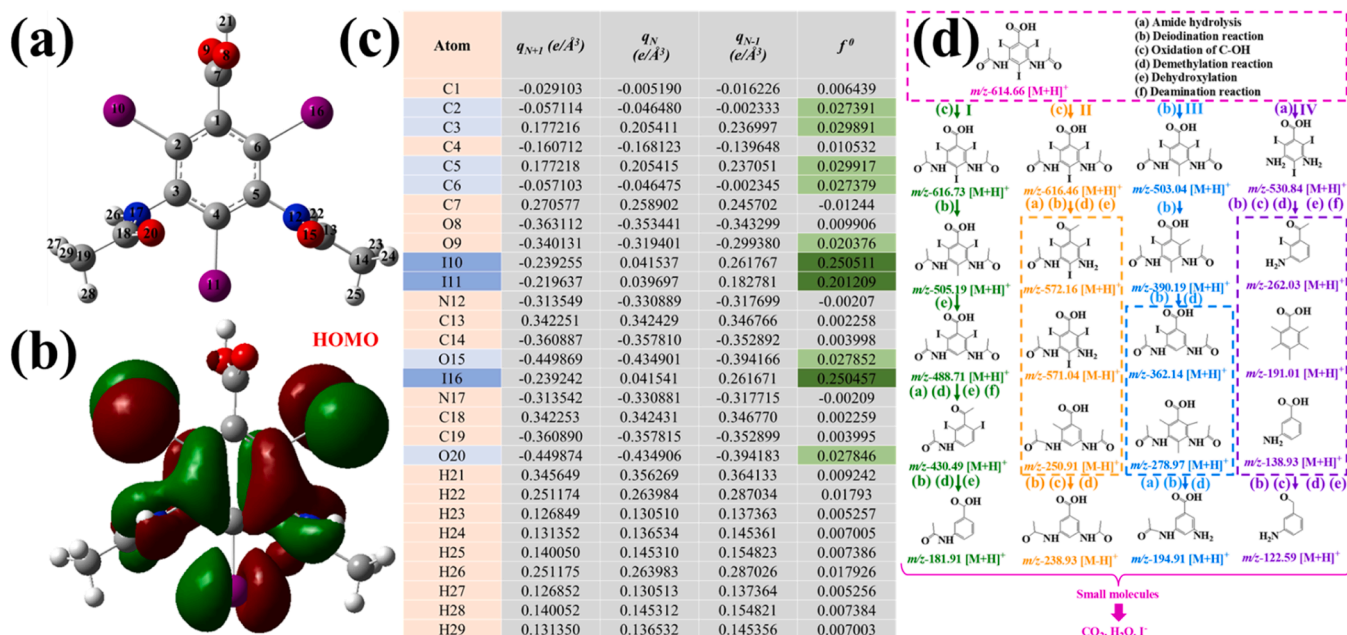


Fig. 4. (a) Chemical structure of DTZ, (b) HOMO of DTZ, (c) DTZ charge distributions and Fukui index ( $f^0$ ) of DTZ, and (d) degradation pathways of DTZ in 2D FeSe<sub>2</sub> @C NS/PMS system.

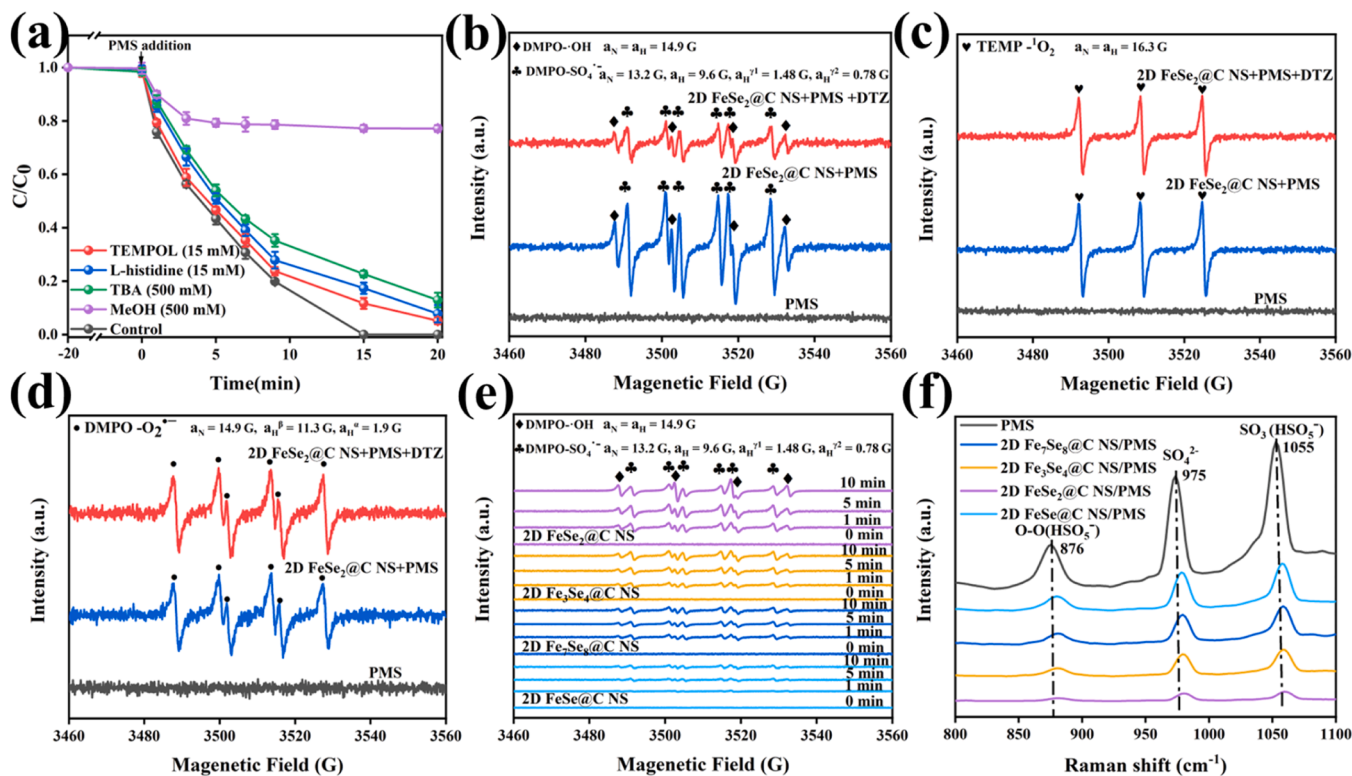


Fig. 5. Degradation of DTZ with quenching reagents in 2D FeSe<sub>2</sub> @C NS/PMS system (a). Reaction conditions: [catalyst]<sub>0</sub> = 0.1 g/L, [PMS]<sub>0</sub> = 1.0 mM, [DTZ]<sub>0</sub> = 10.0 mg/L. EPR spectra under various reaction conditions (b-e), Raman spectra of various reaction systems (f).

catalytic activity order as that of the DTZ degradation. Interestingly, we observed rapid generation of SO<sub>4</sub><sup>•-</sup> and ·OH in 2D FeSe<sub>2</sub>@C NS, 2D Fe<sub>3</sub>Se<sub>4</sub>@C NS, and 2D Fe<sub>7</sub>Se<sub>8</sub>@C NS/PMS systems at the initial stage, but quick saturation. Dissimilarly, those species increase continuously in the 2D FeSe<sub>2</sub>@C NS/PMS system. This explains the rapid degradation of DTZ by 2D FeSe<sub>2</sub>@C NS, 2D Fe<sub>3</sub>Se<sub>4</sub>@C NS, and 2D Fe<sub>7</sub>Se<sub>8</sub>@C NS activated PMS in the initial stage and then flat out quickly, while 2D FeSe<sub>2</sub>@C NS

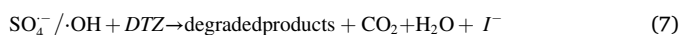
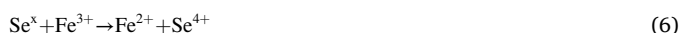
continue to degrade DTZ until a complete removal. Notably, in Fig. S26, both the concentrations of SO<sub>4</sub><sup>•-</sup> and ·OH increased markedly as the PMS concentration increased from 0.5 to 2.0 mM, particularly with the SO<sub>4</sub><sup>•-</sup>. While the peak intensity slightly decreased when the PMS concentration was further increased to 5.0 mM. This phenomenon might be attributed to the self-quenching effect caused by reactions with HSO<sub>5</sub><sup>-</sup> and limited catalyst dosage. However, the above results still prove that 2D FeSe<sub>2</sub>@C



NS are excellent activators of PMS to produce free radicals for pollutant decontamination. Moreover, a mediated electron transfer as the oxidative degradation mechanism [45] can be observed from the linear sweep voltammetry (LSV) tests (Fig. S27(a)) and in-situ Raman (Fig. S27(b)) with accompanying discussions in SI.

Fe complexation experiments with potassium thiocyanate (KSCN) and 2,2'-bipyridine (BPY) were then employed to confirm Fe as the direct active site for ROS production [9,46]. With the existence of KSCN or BPY, the degradation reaction was greatly suppressed (Fig. S28(a-b)). Consistent results can be obtained from the EPR tests (Fig. S29). As SCN<sup>-</sup> or BPY is easily adsorbed onto Fe sites, the critical Fe-poisoning experiment substantiated that the catalytic activity was mainly ascribed to Fe. In addition, the Fe<sup>3+</sup> relative content in 2D FeSe<sub>2</sub>@C NS (Fig. S28(c)) showed a slight increase after reaction, further demonstrating the leading role of Fe sites in activating PMS (see SI for a detailed discussion). Therefore, the catalytic performance of 2D Fe<sub>x</sub>Se<sub>y</sub>@C NS is closely related to the electronic and geometric structure of the Fe active center. Moreover, it can be also concluded that some Se will involve in PMS activation or Fe<sup>2+</sup> palingenesis as an electron donor (Figs. S28(d) and S30(a-c)) (see SI for a detailed discussion).

To further obtain insights into the electron-transfer process at heterogeneous interface for PMS bonding to the catalyst, we determined in-situ Raman spectra (Fig. 5(f)). The peaks at 876, 975, and 1055 cm<sup>-1</sup> are corresponding to the symmetric stretching vibrations of O-O, SO<sub>4</sub><sup>2-</sup>, and SO<sub>3</sub>, respectively, in PMS ([O<sub>3</sub>S-O<sub>1</sub>-O<sub>11</sub>-H]<sup>-</sup>) [2,47]. Therefore, the PMS peak variation can be employed for assessing PMS consumption. After addition of 2D FeSe<sub>2</sub>@C NS, the intensity of PMS drastically decreases, suggesting its decomposition. In addition, compared with 2D FeSe@C NS, 2D Fe<sub>3</sub>Se<sub>4</sub>@C NS, and 2D Fe<sub>7</sub>Se<sub>8</sub>@C NS, the PMS peak intensity becomes the smallest for 2D FeSe<sub>2</sub>@C NS, manifesting its fastest consumption by the catalyst. The cleavage rate of PMS by different catalysts is consistent with the kinetics of DTZ degradation. Evidently, the peaks of PMS stretching vibration display a red-shift to different extents with the presence of a catalyst contrasted to PMS alone, suggesting the charge delivery between PMS and Fe sites. 2D FeSe<sub>2</sub>@C NS show the largest red-shift, indicating that the Fe sites of 2D FeSe<sub>2</sub>@C NS and PMS have stronger affinity. This is very conducive for adsorption of oxygen-containing substances (i.e., PMS) to overcome the inherent limitation for catalytic oxidation. Therefore, based on the above discussions in combination with the previous accounts [8,9,19,41], PMS activation and radical production mechanism can be described in (Eqs. (2)–(7)). In detail, PMS firstly accepts an electron from Fe<sup>2+</sup> on the surface of 2D FeSe<sub>2</sub>@C NS to produce SO<sub>4</sub><sup>•-</sup>. The redox cycle could be achieved through the reaction between Fe<sup>3+</sup> and HSO<sub>5</sub><sup>-</sup> for continuous generation of radicals. Meanwhile, SO<sub>4</sub><sup>•-</sup> could further react with H<sub>2</sub>O to produce ·OH. (Eqs. (2)–(4)). Notably, Se species could also act as an electron donor to promote PMS activation, although this was not the dominant pathway for radical generation (Eq. (5)). More importantly, Fe<sup>3+</sup> would be reduced by Se species with low valence states and quickly regenerate Fe<sup>2+</sup> (Eq. (6)). Finally, SO<sub>4</sub><sup>•-</sup> acts as the main active species to mineralize DTZ into small molecular species (Eq. (7)).



### 3.5. Origin of the enhanced catalytic performance

#### 3.5.1. Spin structures of Fe in catalysts

The excellent intrinsic catalytic activity of 2D FeSe<sub>2</sub>@C NS over 2D FeSe@C NS, 2D Fe<sub>3</sub>Se<sub>4</sub>@C NS, and 2D Fe<sub>7</sub>Se<sub>8</sub>@C NS catalysts may be ascribed to multiple factors, such as material morphology, hydrophilicity, and Fe content. Nevertheless, the similar physicochemical properties of 2D Fe<sub>x</sub>Se<sub>y</sub>@C NS catalysts exclude a predominant influence from the above properties. Meanwhile, the specific surface area and structure defects were also excluded as discussed above. Notably, 2D Fe<sub>x</sub>Se<sub>y</sub>@C NS are d-band catalysts with Fe as the main active center. In this regard, the intrinsic d-orbital electronic properties of Fe affect the catalytic activity. Generally, the electronic properties are strongly linked to the spin structures of Fe [4,48], determining the intrinsic activity of 2D Fe<sub>x</sub>Se<sub>y</sub>@C NS.

Herein, temperature-dependent magnetizations were conducted to study the spin structures of Fe in 2D Fe<sub>x</sub>Se<sub>y</sub>@C NS under field-cooling procedures with a magnetic field of  $H = 1$  kOe for all the samples (Figs. 6(a) and S31(a-d)). An effective magnetic moment ( $\mu_{\text{eff}} = \sqrt{8 C \mu_B}$ ) can be obtained from the fitting results [49,50]. Notably, for a 3d transition metal, the  $\mu_{\text{eff}}$  is generally derived from the spin splitting of partially occupied d orbitals, where  $\mu_{\text{eff}}$  can be calculated by the spin states [48,49]. That is, the order of the spin states is in accordance with that of  $\mu_{\text{eff}}$  values. As displayed in Fig. 6(a), 2D FeSe<sub>2</sub>@C NS exhibited the largest experimental  $\mu_{\text{eff}}$  value (4.16  $\mu_B$ ), followed by 2D Fe<sub>3</sub>Se<sub>4</sub>@C NS (1.84  $\mu_B$ ), 2D Fe<sub>7</sub>Se<sub>8</sub>@C NS (1.30  $\mu_B$ ), and 2D FeSe@C NS (1.07  $\mu_B$ ). Similar results can be further confirmed by their magnetic hysteresis loops (Fig. S32). Notably, it can be observed that the  $\mu_{\text{eff}}$  values of 2D Fe<sub>x</sub>Se<sub>y</sub>@C NS were correlated positively with the  $k_{\text{obs}}$  values, reflecting that the catalytic degradation capacity of 2D Fe<sub>x</sub>Se<sub>y</sub>@C NS is dominated by the Fe spin states (Figs. 6(b) and S33). A larger value of spin-state of 2D Fe<sub>x</sub>Se<sub>y</sub>@C NS leads to higher catalytic activation of PMS. More specifically, a high spin state Fe<sup>2+</sup> serves as the main active site (Fig. S34) (see SI for a detailed discussion). Normally, the e<sub>g</sub> orbitals of a transition metal will be overlapping with O 2p orbitals to participate in  $\sigma$ -bonding with oxygen-containing substances, thus affecting the bonding strength, charge-delivery rates as well as catalytic activity [43, 51]. The high Fe spin-state with large  $\mu_{\text{eff}}$  is conducive to coupling oxygen-containing PMS adsorbates on the metal sites and improves the delivery of spin-oriented charges, thus facilitating PMS adsorption, reinforcing the oxidation potential of the intermediates, and promoting a charge delivery.

#### 3.5.2. Electronic structure and reducibility of the catalysts

To shed light on the role of transition metal surface spin states in PMS activation, we carried out the electrochemical measurements to study the catalyst electronic properties. For a catalyst, the flat band potential ( $E_{\text{FB}}$ ) was calculated from the corresponding intercept of Mott-Schottky curves (Fig. S35), and the  $E_{\text{FB}}$  values of 2D FeSe@C NS, 2D FeSe<sub>2</sub>@C NS, 2D Fe<sub>3</sub>Se<sub>4</sub>@C NS, and 2D Fe<sub>7</sub>Se<sub>8</sub>@C NS are  $-0.90$ ,  $-1.12$ ,  $-0.94$ , and  $-0.92$  V, respectively. Notably, Fermi level can be inferred by  $E_{\text{FB}}$ , and the Fermi level position influences the interface band bend when a catalyst is soaked in reaction solution, deciding the barrier height for charge transfer [8,38]. As revealed in Fig. 7(c), more negative  $E_{\text{FB}}$  of a catalyst reflects a higher location of the Fermi level. Thus, 2D FeSe<sub>2</sub>@C NS with a high spin state Fe are easier to regulate interfacial energetics to reduce electron transfer barriers and give away electrons for PMS activation.

In addition, CV curves disclose the catalyst's redox potential. As depicted in Fig. 7(b), two characteristic peaks (a reduction peak ( $E^{\text{red}}$ ) and an oxidation peak ( $E^{\text{ox}}$ )) present in the CV of catalysts, reflecting the existence of a valence state exchange of Fe<sup>3+</sup>/Fe<sup>2+</sup> in the catalyst [52]. Noticeably, the current intensity of 2D FeSe<sub>2</sub>@C NS is significantly enhanced at  $E^{\text{ox}}$  and  $E^{\text{red}}$  compared to 2D FeSe@C NS, 2D Fe<sub>3</sub>Se<sub>4</sub>@C NS, and 2D Fe<sub>7</sub>Se<sub>8</sub>@C NS, especially for the reduction peak, reflecting that the Fe<sup>3+</sup>/Fe<sup>2+</sup> redox cycling is easily triggered and expedited due to the

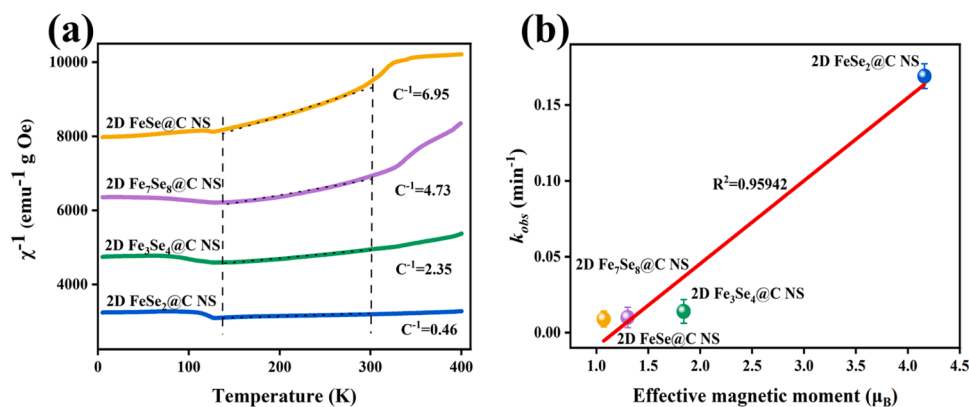


Fig. 6. (a) Temperature dependence inverse susceptibilities ( $C$  is the Curie constant), (b) correlation between  $\mu_{\text{eff}}$  and  $k_{\text{obs}}$  of the as-prepared catalysts.

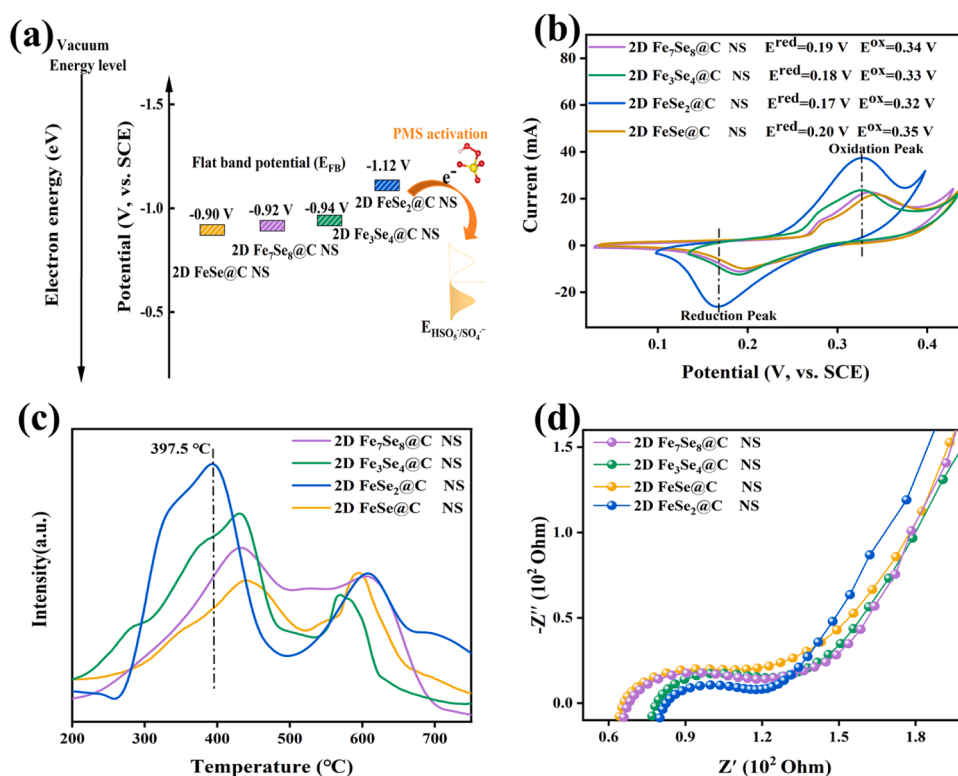


Fig. 7. (a) Flat band potential, (b) cyclic voltammetry (CV) curves, (c) H<sub>2</sub>-TPR profiles, (d) EIS measurements of the as-prepared catalysts.

presence of high spin state Fe sites. Besides, a half-wave potential ( $[E^{\text{red}} + E^{\text{ox}}]/2 = E_{1/2}$ ) on 2D FeSe<sub>2</sub>@C NS (0.25 V) is smaller than that of 2D FeSe@C (0.28 V), Fe<sub>3</sub>Se<sub>4</sub>@C (0.26 V), and Fe<sub>7</sub>Se<sub>8</sub>@C NS (0.27 V), reflecting enhanced Fe<sup>3+</sup> reduction of 2D FeSe<sub>2</sub>@C NS [52]. Therefore, Fe<sup>3+</sup> to Fe<sup>2+</sup> conversion is thermodynamically more favorable for 2D FeSe<sub>2</sub>@C NS than that of 2D FeSe@C NS, 2D Fe<sub>3</sub>Se<sub>4</sub>@C NS, and 2D Fe<sub>7</sub>Se<sub>8</sub>@C NS due to the presence of high spin state Fe. The reduction properties of the catalyst can be further obtained from H<sub>2</sub>-TPR. As displayed in Fig. 7(c), two characteristic peaks at 397.5 and 613.6 °C in the H<sub>2</sub>-TPR curve of 2D FeSe<sub>2</sub>@C NS, indexing as the reduction of Fe<sup>3+</sup> to Fe<sup>2+</sup> and Fe<sup>2+</sup> to Fe, respectively, exhibit higher peak intensities and the peak at 397.5 °C obviously shifts to lower temperature compared to 2D FeSe@C NS, 2D Fe<sub>3</sub>Se<sub>4</sub>@C NS, and 2D Fe<sub>7</sub>Se<sub>8</sub>@C NS. Therefore, it further reflects that the presence of high spin Fe will enhance the reducibility of the catalyst, which facilitates the enhancement of catalytic activity in PMS activation.

Furthermore, the interfacial electron transfer on catalysts can be

studied via electrochemical impedance spectroscopy (EIS). As illustrated in Fig. 7(d), 2D FeSe<sub>2</sub>@C NS present a smaller Nyquist plot diameter, reflecting their better conductivity and charge transfer capacity compared with 2D FeSe@C NS, 2D Fe<sub>3</sub>Se<sub>4</sub>@C NS, and 2D Fe<sub>7</sub>Se<sub>8</sub>@C NS [8]. The higher electron transfer efficiency of 2D FeSe<sub>2</sub>@C NS is also observed in the Tafel curve (Fig. S36) [53].

### 3.5.3. Theoretical calculations

To further understand the spin-state effect of Fe in d-band catalysts, we conducted DFT calculations. The optimal structures of 2D Fe<sub>x</sub>Se<sub>y</sub>@C NS are displayed in Fig. S37(a-d). As depicted in Fig. 8(a), 2D FeSe<sub>2</sub>@C NS present an overt charge depletion around Se and charge accumulation around Fe as contrasted to those in 2D FeSe@C NS, 2D Fe<sub>3</sub>Se<sub>4</sub>@C NS, and 2D Fe<sub>7</sub>Se<sub>8</sub>@C NS systems. The results reflect that the electronic structures of both Fe and Se are regulated and display strong interaction with each other in the 2D FeSe<sub>2</sub>@C NS, which is verified by the XPS results. More specifically, the Bader charge analysis (Fig. 8(a)) shows 2D

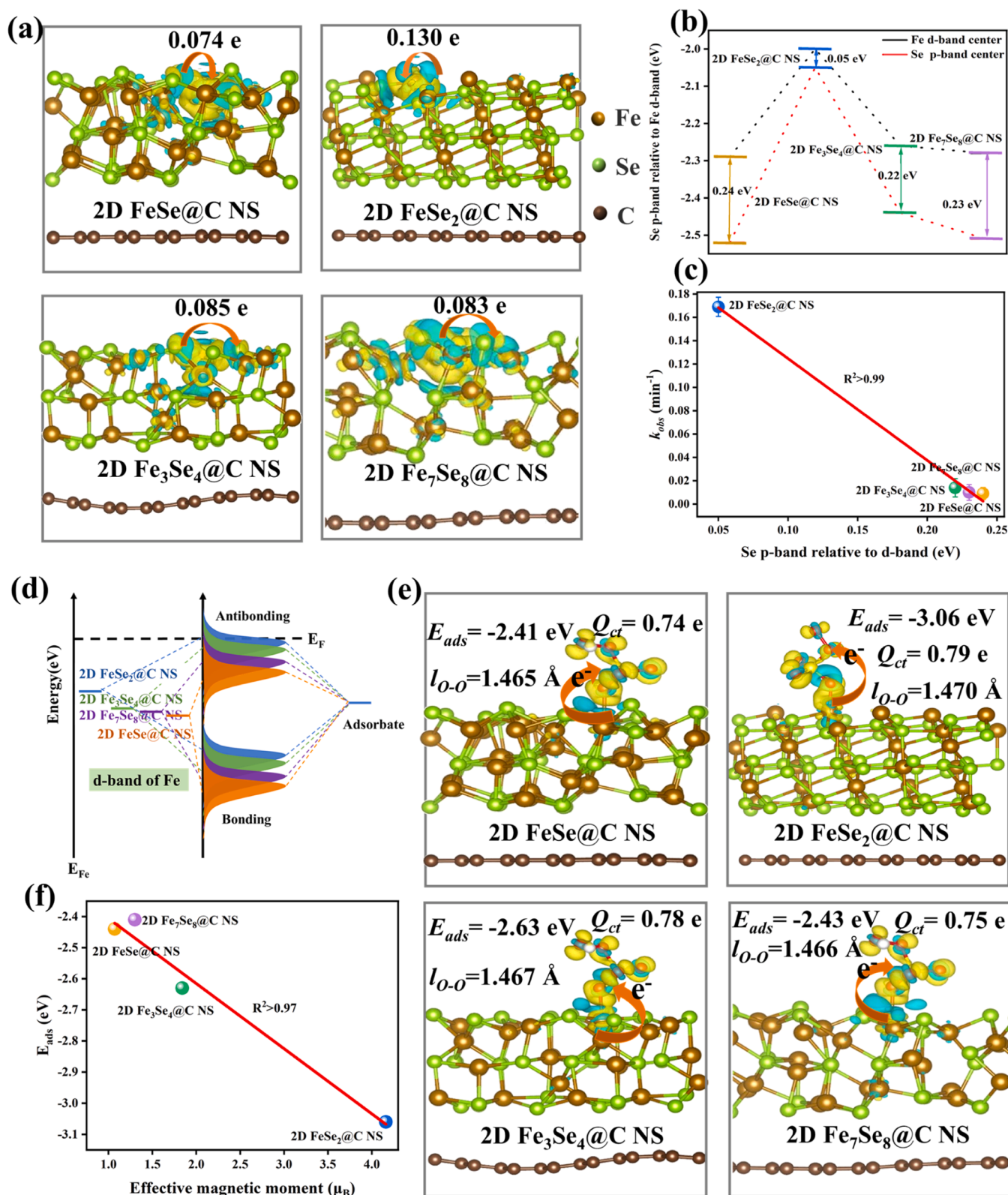


**Fig. 8.** (a) Different charge densities of the four iron-based selenide catalysts, (b) Se p-band center relative to Fe d-band center. (c) Correlation of the  $k_{obs}$  and the Se p-band center relative to Fe d-band center of the four iron-based selenide catalysts in PMS activation. (d) Schematic bond formation between the adsorbate and the catalyst surface. (e) The charge density difference after PMS adsorption on the iron-based selenide catalysts. (The white, yellow and red spheres are referred to H, S and O atoms, respectively). (f) Correlation between  $\mu_{eff}$  and  $E_{ads}$ .



FeSe<sub>2</sub>@C NS have an electron transfer from Se to Fe at 0.13 e, while 2D FeSe@C NS, 2D Fe<sub>3</sub>Se<sub>4</sub>@C NS, and 2D Fe<sub>7</sub>Se<sub>8</sub>@C NS have 0.074, 0.085, and 0.073 e, respectively, reflecting more beneficially for Fe species in 2D FeSe<sub>2</sub>@C NS to trigger the reduction reactions.

Interestingly, when comparing  $k_{obs}$  and the energy difference of Fe d-band relative to the Se p-band center (Figs. 8(b-c) and S38(a-d)), the Fe-Se covalency shows a positive correlation with the  $k_{obs}$  of catalysts. Thus, the interaction of Fe and Se in 2D FeSe<sub>2</sub>@C NS leads to the expansion of Fe-Se covalency, resulting in the presence of high spin state Fe to boost PMS activation via electron transfer. Moreover, the Fe electron delocalization in 2D FeSe<sub>2</sub>@C NS is at a higher degree as compared to that in 2D FeSe@C NS, 2D Fe<sub>3</sub>Se<sub>4</sub>@C NS, and 2D Fe<sub>7</sub>Se<sub>8</sub>@C NS (Fig. S39(a-d)). To validate the speculation, the Kelvin probe force microscopy was used for surface charge density (Fig. S40(a-d)). 2D FeSe<sub>2</sub>@C NS show higher surface potential ( $\Delta E = 410$  mV) than that of 2D FeSe@C NS, 2D Fe<sub>3</sub>Se<sub>4</sub>@C NS, and 2D Fe<sub>7</sub>Se<sub>8</sub>@C NS, further revealing that the 2D FeSe<sub>2</sub>@C NS has high reducibility.

Moreover, among 2D Fe<sub>x</sub>Se<sub>y</sub>@C NS catalysts, 2D FeSe<sub>2</sub>@C NS possess the highest level of d-band center ( $\epsilon_d$ ) at  $-2.00$  eV (Fig. S38(a-d)). The higher of  $\epsilon_d$  energy level, the stronger of the electronic interaction between the catalyst surface and oxygen-containing intermediates is, owing to more charges filling the antibonding state for the adsorption of PMS on Fe-sites [54]. Fig. 8(d) indicates that the antibonding state of 2D FeSe<sub>2</sub>@C NS is higher than that of 2D FeSe@C NS, 2D Fe<sub>3</sub>Se<sub>4</sub>@C NS, and 2D Fe<sub>7</sub>Se<sub>8</sub>@C NS, which reflects that the interaction between surface Fe and PMS is strengthened and that the charge transfer between them is accelerated as well, thereby improving the PMS binding energy to promote PMS decomposition. A consistent conclusion can be drawn from the temperature-programmed desorption of O<sub>2</sub> (O<sub>2</sub>-TPD) and NH<sub>3</sub> (NH<sub>3</sub>-TPD). O<sub>2</sub>-TPD (Fig. S41(a)) displays that the area of peak I (383.9 °C) corresponding to the release of oxygen adsorbed on Fe in 2D FeSe<sub>2</sub>@C NS is much higher than that in 2D FeSe@C NS, 2D Fe<sub>3</sub>Se<sub>4</sub>@C NS, and 2D Fe<sub>7</sub>Se<sub>8</sub>@C NS. It verifies that the affinity and bonding strength for oxygen-containing species are

facilitated with the presence of high spin state active sites. Similar results can be obtained from NH<sub>3</sub>-TPD (Fig. S41(b)), and the increased surface acidity for 2D FeSe<sub>2</sub>@C NS is also favorable to improve the adsorption of PMS. It is noted that a high affinity towards oxygen-containing species is critical for PMS activation during organics degradation.

Furthermore, Fe with an increased 3d charge transition probability in 2D FeSe<sub>2</sub>@C NS can easily provide electrons in the reaction process, that is, Fe in 2D FeSe<sub>2</sub>@C NS has a higher reactivity. Furthermore, the optimized configurations of PMS adsorbed on the surfaces of four models are depicted in Fig. 8(e). The adsorption energies ( $E_{ads}$ ) on 2D Fe<sub>x</sub>Se<sub>y</sub>@C NS are all negative, demonstrating that the adsorption of PMS is energetically favorable. Notably, the  $E_{ads}$  of PMS on 2D FeSe<sub>2</sub>@C NS is more negative than that on 2D FeSe@C NS, 2D Fe<sub>3</sub>Se<sub>4</sub>@C NS, and 2D Fe<sub>7</sub>Se<sub>8</sub>@C NS, suggesting that the high spin state Fe significantly enhanced the interaction between PMS and active sites. Furthermore, comparing to 2D FeSe@C NS, 2D Fe<sub>3</sub>Se<sub>4</sub>@C NS, and 2D Fe<sub>7</sub>Se<sub>8</sub>@C NS, PMS bonded to 2D FeSe<sub>2</sub>@C NS exhibits the longest peroxide bond length ( $l_{O-O}$ ) and a better charge-transfer performance ( $Q = 0.79$  e) (Fig. 8(e)), revealing that the catalyst with high spin state Fe is more beneficial to the activation and cleavage of HSO<sub>5</sub><sup>-</sup>. Interestingly, a roughly negative linear relationship between  $E_{ads}$  and  $\mu_{eff}$  values was established ( $R^2 > 0.97$ ) (Fig. 8(f), further indicating that the  $\mu_{eff}$  and spin states are the critical factors in regulating the catalytic activity of 2D Fe<sub>x</sub>Se<sub>y</sub>@C NS catalysts for PMS activation.

On account of the above analyses, the spin-state-dependent PMS activation mechanism over 2D Fe<sub>x</sub>Se<sub>y</sub>@C NS is summarized in Fig. 9. PMS is bonded to Fe sites to yield SO<sub>4</sub><sup>•-</sup>, which is relied on the spatial configuration of the d orbital in the Fe sites. The interaction between PMS and Fe sites has spin-state-dependent characteristics. Among 2D Fe<sub>x</sub>Se<sub>y</sub>@C NS, Fe sites with a high-spin state in 2D FeSe<sub>2</sub>@C NS can remarkably promote PMS adsorption and interfacial electron transport. Moreover, due to the stronger super-exchange electron interaction between Fe and Se renders 2D FeSe<sub>2</sub>@C NS higher spin states at the Fe site,

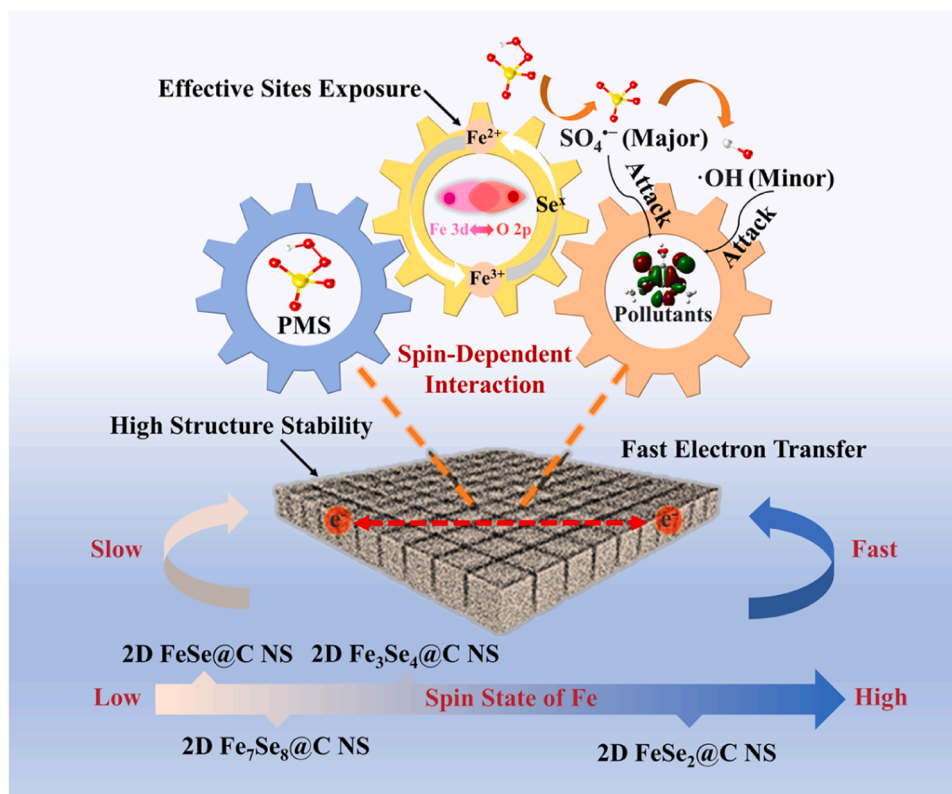


Fig. 9. Catalytic mechanisms of active center spin-dependent catalysts for PMS activation.

the  $\text{Fe}^{3+}/\text{Fe}^{2+}$  redox cycling is easily triggered and expedited. Therefore, a high spin state with a large effective magnetic moment (i.e., 2D  $\text{FeSe}_2$ @C NS) can regulate PMS adsorption for increasing electronic density and accelerate interfacial charge transfer to trigger the efficient PMS activation and DTZ degradation.

#### 4. Conclusion

We have constructed a series of 2D superlattice crystals comprising monolayer iron-based selenide nanocrystals with different crystalline structure through a space-confined topochemical transformation process, and illustrated their superior application in Fenton-like reaction for pollutant degradation. The layered porous structure and 2D geometry of iron-based selenide superlattices render them particularly promising for environmental catalysis. Significantly, among various iron-based selenides (2D  $\text{Fe}_x\text{Se}_y$ @C NS), 2D  $\text{FeSe}_2$ @C NS display the best catalytic performance with excellent stability, adaptability, and good resistance to environmental interference. A 50 mL DTZ solution (10 mg/L) can be degraded within 15 min in the 2D  $\text{FeSe}_2$ @C NS/PMS system, with about 76.8% of the DTZ mineralized after 1 h degradation. In addition, we have also uncovered the nature of catalytic activity of different iron-based selenide nanocrystal superlattices. Systematic experiments and theoretical calculations disclosed that the catalytic activity of different iron-based selenide nanocrystal superlattices is positively correlated ( $R^2 > 0.95$ ) with the high-spin state Fe species (4.16  $\mu_B$ ). The spin-state-dependent mechanism in PMS activation on iron-based selenide nanocrystal superlattices was revealed. This work not only provides the atomic-scale understanding of catalytic trends, highlighting the essential role of the Fe spin state in the PMS activation, but also offers valuable guidance to develop transition metal-based nanocrystal superlattices for future AOP applications in environmental remediation.

#### CRediT authorship contribution statement

**Qiang Zhong:** Conceptualization, Methodology, Investigation, Writing – original draft, Validation, Formal analysis, Visualization, Software. **Yue Sun:** Data curation, Investigation, Software. **Chenmin Xu:** Writing – review & editing, Funding acquisition. **Yanfang Li:** Data curation. **Dunyu Sun:** Data curation. **Leliang Wu:** Data curation. **Shaogui Yang:** Resources, Writing – review & editing, Funding acquisition. **Yazi Liu:** Writing – review & editing. **Chengdu Qi:** Data curation. **Zhe Xu:** Data curation. **Huan He:** Resources, Funding acquisition. **Shiyin Li:** Data curation. **Zun Yao Wang:** Writing – review & editing. **Shaobin Wang:** Writing – review & editing, Formal analysis, Validation.

#### Declaration of Competing Interest

The authors declare that they have no known competing financial interests or personal relationships that could have appeared to influence the work reported in this paper.

#### Data availability

Data will be made available on request.

#### Acknowledgments

This work was supported by the National Nature Science Foundation of China (No. 22206085), the Postgraduate Research & Practice Innovation Program of Jiangsu Province (No. KYCX21\_1399), Major Projects of Jiangsu Provincial Department of Education (23KJA180004), the "Kuncheng Talent" Science and Technology Innovation and Entrepreneurship Leading Talents Program in Changshu and the Qing Lan Project of Jiangsu Province.

#### Appendix A. Supporting information

Supplementary data associated with this article can be found in the online version at doi:10.1016/j.apcatb.2023.123113.

#### References

- [1] J. Lee, U. von Gunten, J.-H. Kim, Persulfate-based advanced oxidation: Critical assessment of opportunities and roadblocks, *Environ. Sci. Technol.* 54 (2020) 3064–3081.
- [2] L. Wu, Z. Sun, Y. Zhen, S. Zhu, C. Yang, J. Lu, Y. Tian, D. Zhong, J. Ma, Oxygen vacancy-induced nonradical degradation of organics: Critical trigger of oxygen ( $\text{O}_2$ ) in the Fe-Co LDH/peroxymonosulfate system, *Environ. Sci. Technol.* 55 (2021) 15400–15411.
- [3] I.A. Ike, K.G. Linden, J.D. Orbell, M. Duke, Critical review of the science and sustainability of persulfate advanced oxidation processes, *Chem. Eng. J.* 338 (2018) 651–669.
- [4] B. Zhang, X. Li, K. Akiyama, P.A. Bingham, S. Kubuki, Elucidating the mechanistic origin of a spin state-dependent  $\text{FeN}_x$ -C catalyst toward organic contaminant oxidation via peroxymonosulfate activation, *Environ. Sci. Technol.* 56 (2022) 1321–1330.
- [5] L.-S. Zhang, X.-H. Jiang, Z.-A. Zhong, L. Tian, Q. Sun, Y.-T. Cui, X. Lu, J.-P. Zou, S.-L. Luo, Carbon nitride supported high-loading Fe single-atom catalyst for activating peroxymonosulfate to generate  $\text{O}_2^{\cdot-}$  with 100% selectivity, *Angew. Chem. Int. Ed.* 60 (2021) 21751–21755.
- [6] G. Zhao, J. Zou, X. Chen, L. Liu, Y. Wang, S. Zhou, X. Long, J. Yu, F. Jiao, Iron-based catalysts for persulfate-based advanced oxidation process: Microstructure, property and tailoring, *Chem. Eng. J.* 421 (2021), 127845.
- [7] H. Zhou, H. Zhang, Y. He, B. Huang, C. Zhou, G. Yao, B. Lai, Critical review of reductant-enhanced peroxide activation processes: Trade-off between accelerated  $\text{Fe}^{3+}/\text{Fe}^{2+}$  cycle and quenching reactions, *Appl. Catal. B-Environ.* 286 (2021), 119900.
- [8] Q. Zhong, C. Xu, Y. Liu, Q. Ji, Z. Xu, D. Sun, S. Zhou, B. Yang, Y. Dai, C. Qi, S. Yang, H. He, S. Li, C. Sun, Defect-engineered  $\text{FeSe}_{2-x}$ @C with porous architecture for enhanced peroxymonosulfate-based advanced oxidation processes, *Appl. Catal. B-Environ.* 309 (2022), 121259.
- [9] G. Fang, T. Zhang, H. Cui, D.D. Dionysiou, C. Liu, J. Gao, Y. Wang, D. Zhou, Synergy between iron and selenide on  $\text{FeSe}_2$ (111) surface driving peroxymonosulfate activation for efficient degradation of pollutants, *Environ. Sci. Technol.* 54 (2020) 15489–15498.
- [10] Y. Deng, X. Xi, Y. Xia, Y. Cao, S. Xue, S. Wan, A. Dong, D. Yang, 2D  $\text{FeP}$  nanoframe superlattices via space-confined topochemical transformation, *Adv. Mater.* 34 (2022) 2109145.
- [11] Y. Deng, Y. Cao, Y. Xia, X. Xi, Y. Wang, W. Jiang, D. Yang, A. Dong, T. Li, Self-templated synthesis of  $\text{CoFeP}$ @C cage-in-cage superlattices for enhanced electrocatalytic water splitting, *Adv. Energy Mater.* 12 (2022) 2202394.
- [12] C. Zhu, D. Du, A. Eychmueller, Y. Lin, Engineering ordered and nonordered porous noble metal nanostructures: synthesis, assembly, and their applications in electrochemistry, *Chem. Rev.* 115 (2015) 8896–8943.
- [13] F. Fetzner, A. Maier, M. Hodas, O. Geladari, K. Braun, A.J. Meixner, F. Schreiber, A. Schnepf, M. Scheele, Structural order enhances charge carrier transport in self-assembled Au-nanoclusters, *Nat. Commun.* 11 (2020) 6188.
- [14] J. Li, Y. Wang, T. Zhou, H. Zhang, X. Sun, J. Tang, L. Zhang, A.M. Al-Enizi, Z. Yang, G. Zheng, Nanoparticle superlattices as efficient bifunctional electrocatalysts for water splitting, *J. Am. Chem. Soc.* 137 (2015) 14305–14312.
- [15] T. Li, B. Xue, B. Wang, G. Guo, D. Han, Y. Yan, A. Dong, Tubular monolayer superlattices of hollow  $\text{Mn}_3\text{O}_4$  nanocrystals and their oxygen reduction activity, *J. Am. Chem. Soc.* 139 (2017) 12133–12136.
- [16] K. Karuppusamy, P. Santhoshkumar, T. Hussain, D. Vikraman, C.-J. Yim, S. Hussain, P. Shanmugam, A. Alfanzani, S. Manickam, H.-S. Kim, Influence of selenide precursors on the formation of iron selenide nanostructures ( $\text{FeSe}_2$ ): Efficient electro-Fenton catalysts for detoxification of harmful organic dyes, *Chemosphere* 272 (2021), 129639.
- [17] M. Wang, Z. Sun, H. Ci, Z. Shi, L. Shen, C. Wei, Y. Ding, X. Yang, J. Sun, Identifying the evolution of Se-vacancy-modulated  $\text{MoSe}_2$  pre-catalyst in Li-S chemistry, *Angew. Chem. Int. Ed.* 60 (2021) 24558–24565.
- [18] M. Yousaf, Z. Wang, Y. Wang, Y. Chen, U. Ali, M. Maqbool, A. Imran, N. Mahmood, P. Gao, R.P.S. Han, Core-shell  $\text{FeSe}_2$ /C nanostructures embedded in a carbon framework as a free standing anode for a sodium ion battery, *Small* 16 (2020) 2002200.
- [19] Q. Zhong, Y. Sun, S. Wu, C. Xu, S. Yang, Y. Liu, D. Sun, B. Yang, Y. Dai, C. Qi, Z. Xu, H. He, S. Li, S. Wang, Uniformed core-shell  $\text{FeSe}_{2-x}$ @C nanocube superlattices for Fenton-like reaction: Coordinative roles of cation and anion, *Appl. Catal. B-Environ.* 325 (2023), 122357.
- [20] M. Ghalawat, P. Poddar, Study of the phase-evolution mechanism of an Fe-Se system at the nanoscale: Optimization of synthesis conditions for the isolation of pure phases and their controlled growth, *Langmuir* 36 (2020) 2012–2022.
- [21] M. Ghalawat, P. Poddar, Remarkable effect of Fe and Se composition on magnetic properties-comparative study of the Fe-Se system at the nanoscale, *J. Phys. Chem. C* 126 (2022) 4655–4663.
- [22] I.S. Lyubutin, C.-R. Lin, K.O. Funtov, T.V. Dmitrieva, S.S. Starchikov, Y.-J. Siao, M.-L. Chen, Structural, magnetic, and electronic properties of iron selenide  $\text{Fe}_{6-7}\text{Se}_8$  nanoparticles obtained by thermal decomposition in high-temperature organic solvents, *J. Chem. Phys.* 141 (2014), 044704.

- [23] X. Mao, J.-G. Kim, J. Han, H.S. Jung, S.G. Lee, N.A. Kotov, J. Lee, Phase-pure FeSe<sub>x</sub> (x=1, 2) nanoparticles with one- and two-photon luminescence, *J. Am. Chem. Soc.* 136 (2014) 7189–7192.
- [24] B. Jang, M. Park, O.B. Chae, S. Park, Y. Kim, S.M. Oh, Y. Piao, T. Hyeon, Direct synthesis of self-assembled ferrite/carbon hybrid nanosheets for high performance lithium-ion battery anodes, *J. Am. Chem. Soc.* 134 (2012) 15010–15015.
- [25] M. Zhang, C. Xiao, X. Yan, S. Chen, C. Wang, R. Luo, J. Qi, X. Sun, L. Wang, J. Li, Efficient removal of organic pollutants by metal-organic framework derived Co/C yolk-shell nanoreactors: Size-exclusion and confinement effect, *Environ. Sci. Technol.* 54 (2020) 10289–10300.
- [26] Z. Xiong, D. Sun, X. Jia, J. Zhou, Core/shell FeSe/carbon nanosheet-assembled micro flowers with ultrahigh coulombic efficiency and rate performance as nonpresodiate anode for sodium-ion battery, *Carbon* 166 (2020) 339–349.
- [27] Q. Pan, M. Zhang, L. Zhang, Y. Li, Y. Li, C. Tan, F. Zheng, Y. Huang, H. Wang, Q. Li, FeSe<sub>2</sub>@C microrods as a superior long-life and high-rate anode for sodium ion batteries, *ACS Nano* 14 (2020) 17683–17692.
- [28] Y. Wang, Y. Zhang, R. Shao, Q. Guo, FeSe and Fe<sub>3</sub>Se<sub>4</sub> encapsulated in mesoporous carbon for flexible solid-state supercapacitor, *Chem. Eng. J.* 442 (2022), 136362.
- [29] X. Xu, J. Liu, L. Liu, L. Ouyang, R. Hu, H. Wang, L. Yang, M. Zhu, A general metal-organic framework (MOF)-derived selenidation strategy for in situ carbon-encapsulated metal selenides as high-rate anodes for Na-ion batteries, *Adv. Funct. Mater.* 28 (2018) 1707583.
- [30] M. Yousaf, Z. Wang, Y. Wang, Y. Chen, U. Ali, M. Maqbool, A. Imran, N. Mahmood, P. Gao, R.P.S. Han, Core-shell FeSe<sub>2</sub>/C nanostructures embedded in a carbon framework as a free standing anode for a sodium ion battery, *Small* 16 (2020) 2002200.
- [31] B. Yuan, W. Luan, S.-t. Tu, One-step synthesis of cubic FeS<sub>2</sub> and flower-like FeSe<sub>2</sub> particles by a solvothermal reduction process, *Dalton Trans.* 41 (2012) 772–776.
- [32] Y. Yao, C. Wang, X. Yan, H. Zhang, C. Xiao, J. Qi, Z. Zhu, Y. Zhou, X. Sun, X. Duan, J. Li, Rational regulation of Co-N-C coordination for high-efficiency generation of O<sub>2</sub> toward nearly 100% selective degradation of organic pollutants, *Environ. Sci. Technol.* 56 (2022) 8833–8843.
- [33] M. Thommes, K. Kaneko, A.V. Neimark, J.P. Olivier, F. Rodriguez-Reinoso, J. Rouquerol, K.S.W. Sing, Physisorption of gases, with special reference to the evaluation of surface area and pore size distribution (IUPAC Technical Report), *Pure Appl. Chem.* 87 (2015) 1051–1069.
- [34] P. Li, Y. Lin, S. Zhao, Y. Fu, W. Li, R. Chen, S. Tian, Defect-engineered Co<sub>3</sub>O<sub>4</sub> with porous multishelled hollow architecture enables boosted advanced oxidation processes, *Appl. Catal. B-Environ.* 298 (2021), 120596.
- [35] C. An, Y. Yuan, B. Zhang, L. Tang, B. Xiao, Z. He, J. Zheng, J. Lu, Graphene wrapped FeSe<sub>2</sub> nano-microspheres with high pseudocapacitive contribution for enhanced Na-ion storage, *Adv. Energy Mater.* 9 (2019) 1900356.
- [36] Y. Lei, X. Guo, M. Jiang, W. Sun, H. He, Y. Chen, K. Thummavichai, O. Ola, Y. Zhu, N. Wang, Co-ZIF reinforced cow manure biochar (CMB) as an effective peroxymonosulfate activator for degradation of carbamazepine, *Appl. Catal. B-Environ.* 319 (2022), 121932.
- [37] M.N. Sugihara, D. Moeller, T. Paul, T.J. Strathmann, TiO<sub>2</sub>-photocatalyzed transformation of the recalcitrant X-ray contrast agent diatrizoate, *Appl. Catal. B-Environ.* 129 (2013) 114–122.
- [38] Z. Xu, Y. Wu, X. Wang, Q. Ji, T. Li, H. He, H. Song, S. Yang, S. Li, S. Yan, L. Zhang, Z. Zou, Identifying the role of oxygen vacancy on cobalt-based perovskites towards peroxymonosulfate activation for efficient iohexol degradation, *Appl. Catal. B-Environ.* 319 (2022), 121901.
- [39] J. Qi, X. Yang, P.-Y. Pan, T. Huang, X. Yang, C.-C. Wang, W. Liu, Interface engineering of Co(OH)<sub>2</sub> nanosheets growing on the KNbO<sub>3</sub> perovskite based on electronic structure modulation for enhanced peroxymonosulfate activation, *Environ. Sci. Technol.* 56 (2022) 5200–5212.
- [40] P. Zhang, Y. Yang, X. Duan, Y. Liu, S. Wang, Density functional theory calculations for insight into the heterocatalyst reactivity and mechanism in persulfate-based advanced oxidation reactions, *ACS Catal.* 11 (2021) 11129–11159.
- [41] P. Duan, Y. Qi, S. Feng, X. Peng, W. Wang, Y. Yue, Y. Shang, Y. Li, B. Gao, X. Xu, Enhanced degradation of clothianidin in peroxymonosulfate/catalyst system via core-shell FeMn@N-C and phosphate surrounding, *Appl. Catal. B-Environ.* 267 (2020), 118717.
- [42] W. Du, Q. Zhang, Y. Shang, W. Wang, Q. Li, Q. Yue, B. Gao, X. Xu, Sulfate saturated biosorbent-derived Co-S@NC nanoarchitecture as an efficient catalyst for peroxymonosulfate activation, *Appl. Catal. B-Environ.* 262 (2020), 118302.
- [43] Z.-Y. Guo, C.-X. Li, M. Gao, X. Han, Y.-J. Zhang, W.-J. Zhang, W.-W. Li, Mn-O covalency governs the intrinsic activity of Co-Mn spinel oxides for boosted peroxymonosulfate activation, *Angew. Chem. Int. Ed.* 60 (2021) 274–280.
- [44] N. Li, R. Li, X. Duan, B. Yan, W. Liu, Z. Cheng, G. Chen, La Hou, S. Wang, Correlation of active sites to generated reactive species and degradation routes of organics in peroxymonosulfate activation by Co-loaded carbon, *Environ. Sci. Technol.* 55 (2021) 16163–16174.
- [45] P. Shao, Y. Jing, X. Duan, H. Lin, L. Yang, W. Ren, F. Deng, B. Li, X. Luo, S. Wang, Revisiting the graphitized nanodiamond-mediated activation of peroxymonosulfate: Singlet oxygenation versus electron transfer, *Environ. Sci. Technol.* 55 (2021) 16078–16087.
- [46] Y. Gao, T. Wu, C. Yang, C. Ma, Z. Zhao, Z. Wu, S. Cao, W. Geng, Y. Wang, Y. Yao, Y. Zhang, C. Cheng, Activity trends and mechanisms in peroxymonosulfate-assisted catalytic production of singlet oxygen over atomic metal-N-C catalysts, *Angew. Chem. Int. Ed.* 60 (2021) 22513–22521.
- [47] Y. Si, Z.-Y. Guo, Y. Meng, H.-H. Li, L. Chen, A.-Y. Zhang, C.-H. Gu, W.-W. Li, H.-Q. Yu, Reusing sulfur-poisoned palladium waste as a highly active, nonradical fenton-like catalyst for selective degradation of phenolic pollutants, *Environ. Sci. Technol.* 56 (2022) 564–574.
- [48] G. Shen, R. Zhang, L. Pan, F. Hou, Y. Zhao, Z. Shen, W. Mi, C. Shi, Q. Wang, X. Zhang, J.-J. Zou, Regulating the spin state of Fe<sup>II</sup> by atomically anchoring on ultrathin titanium dioxide for efficient oxygen evolution electrocatalysis, *Angew. Chem. Int. Ed.* 59 (2020) 2313–2317.
- [49] S. Zhou, X. Miao, X. Zhao, C. Ma, Y. Qiu, Z. Hu, J. Zhao, L. Shi, J. Zeng, Engineering electrocatalytic activity in nanosized perovskite cobaltite through surface spin-state transition, *Nat. Commun.* 7 (2016) 11510.
- [50] S. Sun, G. Shen, J. Jiang, W. Mi, X. Liu, L. Pan, X. Zhang, J.-J. Zou, Boosting oxygen evolution kinetics by Mn-N-C motifs with tunable spin state for highly efficient solar-driven water splitting, *Adv. Energy Mater.* 9 (2019) 1901505.
- [51] T. Zhang, G.V. Lowry, N.L. Capiro, J. Chen, W. Chen, Y. Chen, D.D. Dionysiou, D. W. Elliott, S. Ghoshal, T. Hofmann, H. Hsu-Kim, J. Hughes, C. Jiang, G. Jiang, C. Jing, M. Kavanaugh, Q. Li, S. Liu, J. Ma, B. Pan, T. Phenrat, X. Qu, X. Quan, N. Saleh, P.J. Vikesland, Q. Wang, P. Westerhoff, M.S. Wong, T. Xia, B. Xing, B. Yan, L. Zhang, D. Zhou, P.J.J. Alvarez, In situ remediation of subsurface contamination: opportunities and challenges for nanotechnology and advanced materials, *Environ. Sci. -Nano* 6 (2019) 1283–1302.
- [52] T. Li, Y. Chen, X. Wang, J. Liang, L. Zhou, Modifying organic carbon in Fe<sub>3</sub>O<sub>4</sub>-loaded schwertmannite to improve heterogeneous Fenton activity through accelerating Fe(II) generation, *Appl. Catal. B-Environ.* 285 (2021), 119830.
- [53] Z. Wu, Y. Wang, Z. Xiong, Z. Ao, S. Pu, G. Yao, B. Lai, Core-shell magnetic Fe<sub>3</sub>O<sub>4</sub>@Zn/Co-ZIFs to activate peroxymonosulfate for highly efficient degradation of carbamazepine, *Appl. Catal. B-Environ.* 277 (2020), 119136.
- [54] J. Wu, X. Wang, W. Zheng, Y. Sun, Y. Xie, K. Ma, Z. Zhang, Q. Liao, Z. Tian, Z. Kang, Y. Zhang, Identifying and interpreting geometric configuration-dependent activity of spinel catalysts for water reduction, *J. Am. Chem. Soc.* 144 (2022) 19163–19172.